Chapter 17

Coronal Mass Ejections (CMEs)

Every star is losing mass, caused by dynamic phenomena in its atmosphere that accelerate plasma or particles beyond the escape speed. Inspecting the Sun, our nearest star, we observe two forms of mass loss: the steady *solar wind outflow* and the sporadic ejection of large plasma structures, termed *coronal mass ejections (CMEs)*. The solar wind outflow amounts to $\approx 2 \times 10^{-10}$ (g cm^{-2} s^{-1}) in coronal holes, and to $\lesssim 4 \times 10^{-11}$ (g cm^{-2} s^{-1}) in active regions. The phenomenon of a CME occurs with a frequency of about 1 event per day, carrying a mass in the range of $m_{CME} \approx 10^{14} - 10^{16}$ g, which corresponds to an average mass loss rate of $m_{CME}/(\Delta t \cdot 4\pi R_\odot^2) \approx 2 \times 10^{-14} - 2 \times 10^{-12}$ (g cm^{-2} s^{-1}), which is $\lesssim 1\%$ of the solar wind mass loss in coronal holes, or $\lesssim 10\%$ of the solar wind mass in active regions. The transverse size of CMEs can cover from a fraction up to more than a solar radius, and the ejection speed is in the range of $\mathrm{v}_{CME} \approx 10^2 - 10^3$ (km s^{-1}). A CME structure can have the geometric shape of a fluxrope, a semi-shell, or a bubble, which is the subject of much debate, because of ambiguities from line-of-sight projection effects and the optical thinness. There is a general consensus that a CME is associated with a release of magnetic energy in the solar corona, but its relation to the flare phenomenon is controversial. Even big flares (at least GOES M-class) have no associated CMEs in 40% of the cases (Andrews 2003). A long-standing debate focused on the question of whether a CME is a by-product of the flare process or vice versa. This question has been settled in the view that both CMEs and flares are quite distinct and independent plasma processes, although related to each other, because both are by-products of a common magnetic instability controlled on a larger global scale. A CME is a dynamically evolving plasma structure, propagating outward from the Sun into interplanetary space, carrying a frozen-in magnetic flux and expanding in size. If a CME structure travels towards the Earth, which is mostly the case when launched in the western solar hemisphere, due to the curvature of the *Parker spiral* interplanetary magnetic field, such an *Earth-directed* event can engulf the Earth's magnetosphere and generate significant geomagnetic storms. Obviously such geomagnetic storms can cause disruptions of global communication and navigation networks, can cause failures of satellites and commercial power systems, and thus are subject of high interest.

Reviews on CMEs can be found in MacQueen (1980), Howard et al. (1985), Kahler

(1987, 1992), Low (1994, 1996, 2001a), Hundhausen (1999), Forbes (2000c), Klimchuk (2001), Cargill (2001), or in the monographs and proceedings of Crooker et al. (1997), Low (1999a), and Daglis (2001).

17.1 Theoretical Concepts of CMEs

The physical concept of various theoretical CME models can perhaps be best understood in terms of mechanical analogues, as shown in Fig. 17.1. We summarize the essential concepts of five major CME models, following the theoretical review by Klimchuk (2001), see also Low (1999b, 2001a,b).

17.1.1 Thermal Blast Model

Early models proposed that the driving force of a CME is caused by a greatly enhanced thermal pressure, produced by a flare, which cannot be contained by the magnetic field and thus pushes the CME outward into the heliosphere (Dryer 1982; Wu 1982). An analogue to the thermal blast model is the overpressure generated by a bomb explosion (Fig. 17.1, top panel). So, the flare was initially thought to be the primary trigger of a CME. In the meantime, however, many CMEs have been recorded without a preceding flare, or the timing was found such that the CME launch occurred first, and flare-related emission later (e.g., Harrison 1986). Thus, today we think that the thermal blast model cannot be correct in many CME events, although the relative timing is sometimes very close (e.g., Dryer 1996; Délannée et al. 2000; Zhang et al. 2001b). A recent MHD simulation that employed hot plasma injection as a driver mechanism of a fluxrope eruption found that this model could not reproduce the interplanetary magnetic cloud data over the range of $0.4 - 5$ AU (Krall et al. 2000).

17.1.2 Dynamo Model

The class of dynamo-driven CME models implies a rapid generation of magnetic flux by real-time stressing of the magnetic field. A mechanical analogue is the stressing of a spring by an external force (Fig. 17.1, second panel). In the solar application, the driver of magnetic stressing is accomplished by an external force (e.g., by rapid displacements of the footpoints of a coronal magnetic field system). A theoretical study demonstrated that shearing of a coronal loop arcade always leads to an inflation of the entire magnetic field (Klimchuk 1990), and thus a sufficiently fast driver is expected to produce a CME-like expulsion. In recent simulations (Chen 1989, 1997a, 2000; Krall et al. 2000) such a driver mechanism is called *flux injection*, which corresponds to one of the three scenarios: (1) pre-existing coronal field lines become twisted, (2) new ring-shaped field lines rise upward in the corona while becoming detached from the photosphere, or (3) new arch-shaped field lines emerge into the corona while staying anchored at their photospheric footpoints. The problem with the first scenario is that the required footpoint motion has to be at least two orders of magnitude faster than the observed one (e.g., Krall et al. 2000). Also the second scenario is unlikely because the amount of entrained mass has never been observed and no obvious forces exist

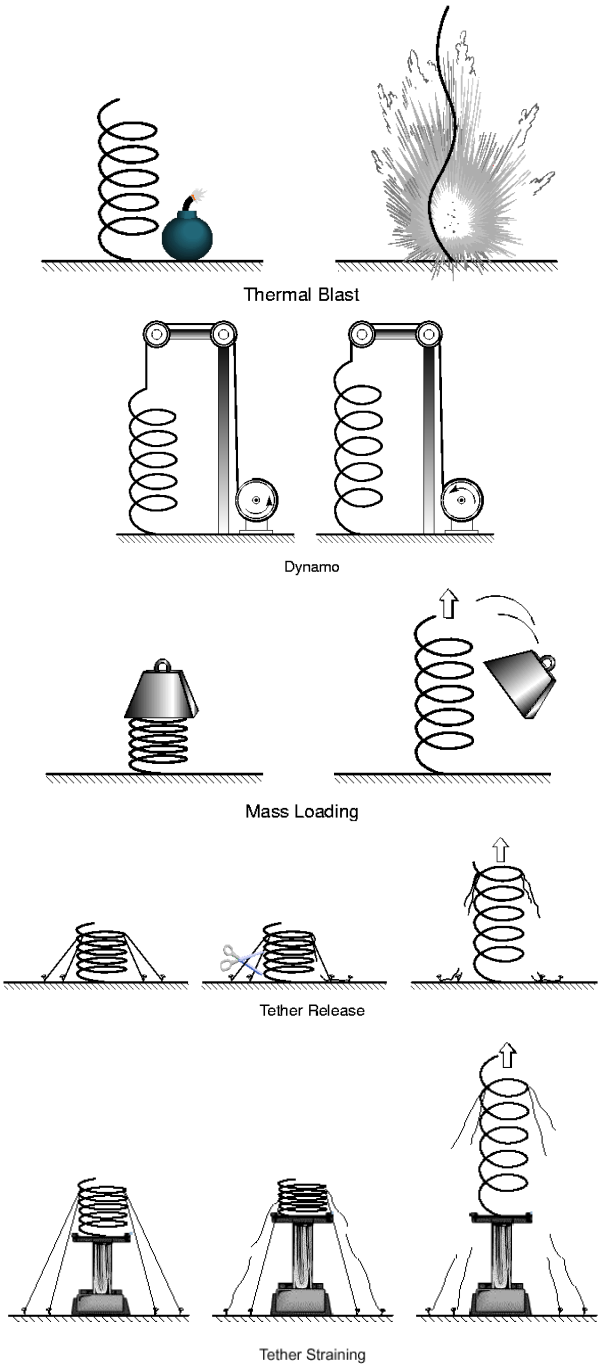

Figure 17.1: Physical (mechanical) analogues of five different *coronal mass ejection (CME)* models: (a) thermal blast model, (b) dynamo model, (c) mass loading model, (d) tether cutting model, and (e) tether straining model (Klimchuk 2001).

to lift the mass. The third possibility with emerging flux is more likely, but there are issues whether the required increase of vertical flux through the photosphere is consistent with observations. Blackman & Brandenburg (2003) suggest that the launch of CMEs balances the conservation of magnetic helicity during the solar cycle, by simultaneously liberating small-scale twist and large-scale writhe of opposite sign.

17.1.3 Mass Loading Model

The next three CME models are also called *storage and release models*, which entail a slow build-up of magnetic stress before eruption begins. One of them is loading with mass (see the analogue of a spring that is compressed by a heavy weight and explosively uncoils when the weight is shifted to one side, Fig. 17.1, middle panel). The mass loading process during the pre-eruption phase of a CME can be manifested in the form of a growing quiescent or eruptive filament (§ 6.4), for instance. Theoretical studies compare the total magnetic energy in pre-eruption and posteruption equilibrium configurations in order to demonstrate the plausible transition from a higher to a lower energy state (Low & Smith 1993; Chou & Charbonneau 1996; Wolfson & Dlamini 1997; Wolfson & Saran 1998; Guo & Wu 1998; Low 1999a). There are two forms of mass loading: (1) by prominences, which are extremely dense, contained in a compact volume, and of chromospheric temperature; and (2) by a relatively higher electron density distributed over a large volume, which is unstable to the Rayleigh−Taylor or Kruskal−Schwarzschild instability, if it overlays a volume of lower density. The first concept that prominences play a fundamental role in the launch of CMEs (Low 1996, 1999a) is supported by the observations with coincident starts of prominences and CMEs. A crucial criterion is the mass of the prominence (Low et al. 2003, Zhang & Low 2004). The second concept of unstable mass loading over a larger volume is supported by observations of CMEs from helmet streamers that contain lower density cavities (Hundhausen 1988, 1999), but there are also numerous counter-examples without any signs of internal low-density regions.

17.1.4 Tether Release Model

As we discussed in § 6.2.2, magnetically dominated configurations like coronal loops generally involve a balance between the upward-directed force of magnetic pressure, $-\nabla(p + B^2/8\pi)$, and the downward-directed force of magnetic tension, $(1/4\pi)(\mathbf{B} \cdot \nabla)\mathbf{B}$. The field lines that provide the tension are sometimes called *tethers*, analogous to the ground-anchored ropes that hold down a buoyant balloon. In our mechanical analogy, the tether ropes hold down a compressed spring (Fig. 17.1, forth panel). Once the tethers are released one after the other, the tension on the remaining thethers increases, until the strain becomes eventually so large that the remaining thethers start to break and the spring uncoils in a catastrophic explosion. This process has been dubbed *tether release*, while the earlier term *tether cutting* refers more to the explosive end phase. A 2D model (with translational symmetry) has been developed which demonstrates how a tether release may work in the solar corona (Forbes & Isenberg 1991; Isenberg et al. 1993; Lin et al. 1998a; Van Tend & Kuperus 1978; Van Ballegooijen & Martens 1989). We described the loss-of-equilibrium model of Forbes & Priest

(1995) in § 10.5.3, which is a transition through a sequence of equilibria, driven by converging footpoint motion, until a loss of equilibrium occurs and the X-point jumps discontinuously upward into a new equilibrium position. In a non-ideal MHD situation, where enhanced resistivity is present in the X-point, an eruption with a launch of a CME would result, after break-off of the "tethers" during the loss-of-equilibrium phase (Forbes 1991; Lin & Forbes 2000; Mikić & Linker 1999; Amari et al. 2000).

17.1.5 Tether Straining Model

The *tether straining model* is similar to the *tether release model*, except that the strain on the tethers gradually increases by some external force until they brake, while the force on the tethers is constant in the former model, but is distributed to fewer and fewer tethers with time until they brake. One physical model of the tether-straining class is the *magnetic breakout model* of Antiochos (1998) and Antiochos et al. (1999b), described in § 10.5.5 (Fig. 10.26). The magnetic breakout model is a quadrupolar structure with two adjacent arcades, having overarching magnetic field lines over the whole system that represent the tethers. One loop arcade is continuously sheared and builds up magnetic stress until magnetic reconnection starts in the overlying X-point between the two loop arcades. The magnetic reconnection process then opens up the magnetic field in an upward direction (i.e., the "break-up" phase), and allows the CME to escape into interplanetary space. There are variants of this magnetic breakout model. A similar breakout effect can also be achieved in a bipolar magnetic field with the mass loading model (Low & Zhang 2002; Zhang et al. 2002). While the original model of Antiochos et al. (1999b) is 2D and symmetric, the version of Aulanier et al. (2000a) involves 3D nullpoints with a separatrix dome beneath the 3D nullpoint and a spine field line above (Plate 13), which can be an open field line (Fig. 10.26) and then marks the escape route of the CME. Another thether-straining model is the equilibrium-loss model of Forbes & Priest (1995), described in § 10.5.3. The straining driver is given by the converging footpoint motion and magnetic reconnection is initialized underneath the erupting structure, while it occurs above the erupting structure in the magnetic breakout model. Other examples of tether-straining models are the sheared arcade models of Mikić & Linker (1994b), Linker & Mikić (1995), Choe & Lee (1996), and Amari et al. (1996), and the fluxrope models of Wu et al. (1995) and Wu et al. (2000).

17.2 Numerical MHD Simulations of CMEs

There are two kinds of theoretical simulations on CMEs: (1) analytical time-dependent MHD models, which provide insights into the physical mechanisms, but cannot reproduce the detailed morphology of the observations; and (2) numerical time-dependent MHD simulations, which should be able to reproduce the observations if sufficiently accurate initial conditions and boundary conditions are known. Reviews on the theoretical modeling of CMEs can be found in Low (2001b), and a review on numerical MHD modeling of CMEs in Wu et al. (2001).

17.2.1 Analytical Models of CMEs

The general framework of the ideal and resistive MHD equations is given in § 6.1.3 and § 6.1.5. The simplest description of a CME in fully developed motion was modeled analytically with the one-fluid MHD equations including gravity, but avoiding the complicated energy equation, but instead using the polytropic assumption with an index of $\gamma < 5/3$. The MHD equations for a polytropic index of $\gamma = 4/3$ yield a family of self-similar solutions in 2D and 3D space (Gibson & Low 1998; Low 2001b). In this model, the mass expulsion in the gravitational potential well yields an almost constant or mildly accelerated propagation speed for CMEs, after the hydromagnetic system becomes gravitationally unstable (Low et al. 1982; Low 1984b). Kinematic models with raising filaments that increase the magnetic pressure under a helmet streamer and drive the outward motion have been presented by Pneuman (1980) and Van Tend (1979). Photospheric flows as drivers of CMEs have been considered by Biskamp & Welter (1989). The energetics and causes of CMEs in terms of fluxrope geometries have been studied by Forbes & Isenberg (1991) and Chen (1997a). Analytical solutions of the time-dependent MHD equations that describe the expulsion of a CME have been calculated by Gibson & Low (1998). Low (1984) pointed out that the launch of a CME is a two-step process, consisting of (1) an initial phase where the closed coronal magnetic field is opened up to eject the trapped (prominence) material, which can be an ideal MHD process, and (2) a second phase involving magnetic reconnection of the open field lines beneath the erupted structure, which is a dissipative or resistive MHD process. A further refinement along the same basic evolution is the *magnetic breakout model* of Antiochos (1998) and Antiochos et al. (1999b), although it has not been modeled analytically.

17.2.2 Numerical MHD Simulations of CMEs

A more general approach is to solve the MHD equations with a numerical code, starting from an initial condition and propagating in time, with a least two dimensions in space. There are three generations of numerical MHD simulations of CMEs, based on (1) thermal blast models, (2) helmet streamer configurations, and (3) magnetic fluxrope configurations.

The first generation of numerical MHD models of CMEs assumed the initial corona to be static and potential (i.e., current free) or force-free (i.e., current-aligned) fields, where a pressure pulse was introduced to mimic a flare energy release (Nakagawa et al. 1978, 1981; Dryer et al. 1979; Steinolfson et al. 1978; Wu et al. 1978, 1982). The deficiency of this model is that neither the initial state nor the driver (thermal blast model, § 17.1.1) is realistic and consequently the model cannot reproduce observed morphological features of CMEs (Dryer 1994; Wu et al. 2001).

The second generation of numerical MHD models of CMEs (Steinolfson & Hundhausen 1988; Steinolfson 1992; Mikić et al. 1988; Guo et al. 1992; Wang et al. 1995b; Wu et al. 2000; see example in Fig. 17.2) assume a coronal helmet streamer to be the magnetic configuration of the initial state, where a CME originates from the disruption of global-scale streamers (Illing & Hundhausen 1986; Dere et al. 1997b; Subramanian et al. 1999; Plunkett et al. 2000). This generation of MHD simulations succeded to

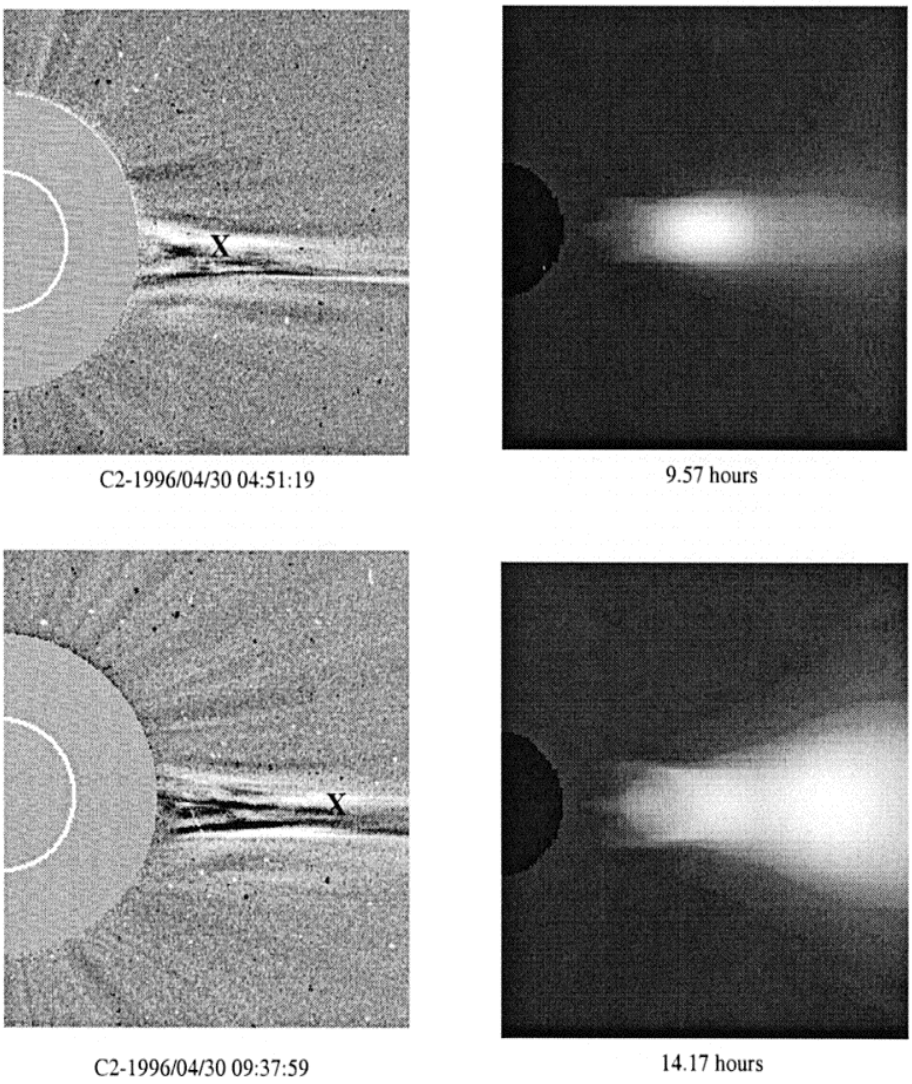

Figure 17.2: Numerical MHD simulation of a CME with the helmet streamer model is shown in the right panels. A comparison with the observed running difference images of an outward plasma blob, observed with SoHO/LASCO on 1996-Apr-30, 04:51 UT and 09:37 UT, is shown in the left panels. Note that the centroid of the plasma blob (marked with a cross in the left panels) coincides with the centroid in the MHD simulations (Wu et al. 2000).

reproduce a loop-like CME (Steinolfson & Hundhausen 1988) and to reproduce the observed three-part structure: (1) a bright front or leading edge (the pre-eruption helmet structure), surrounding (2) a dark cavity, which contains (3) a bright core, identified as a helical prominence (Hundhausen 1988, 1999; Guo & Wu 1998). MHD simula-

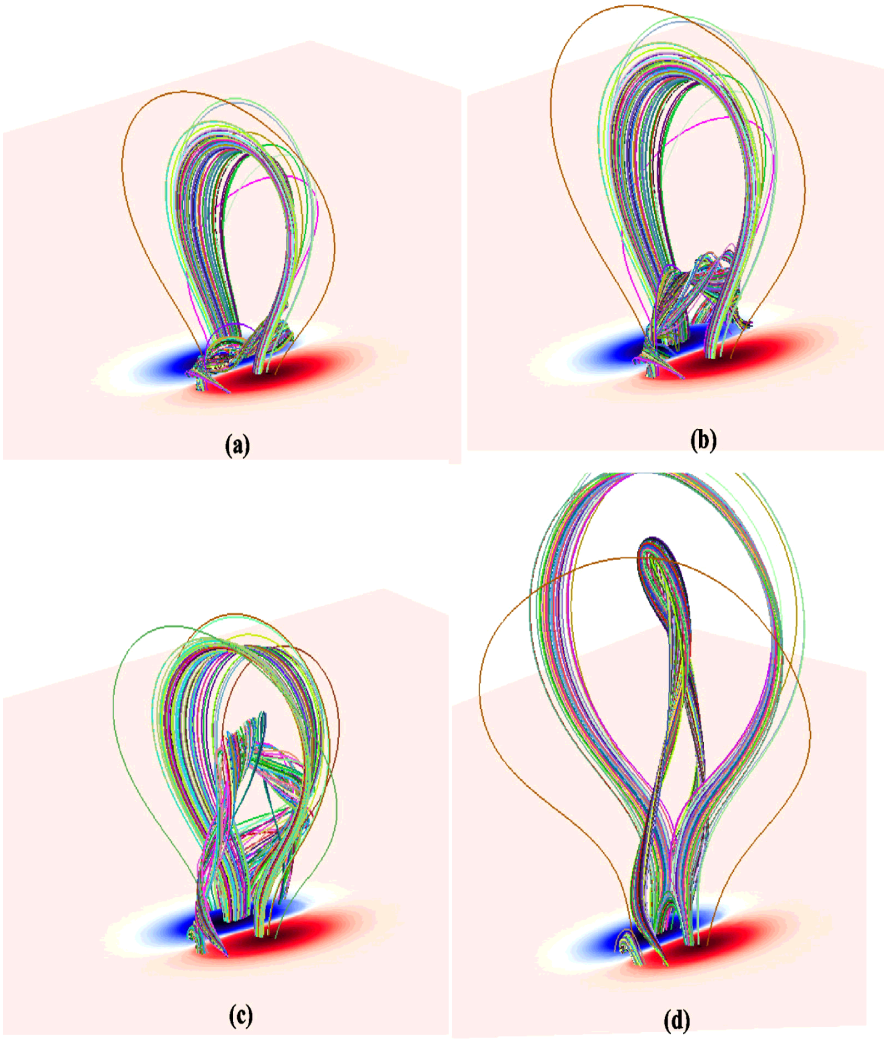

Figure 17.3: Numerical MHD simulation of the evolution of a CME, driven by turbulent diffusion. The four panels correspond to the times (a) t=850, (b) t=950, (c) t=1050, and (d) t=1150, where viscous relaxation is started at t=850, triggering a global disruption involving opening, reconnection through the overlying arcade and below, and the formation of a current sheet, associated with a high dissipation of magnetic energy and a strong increase of kinetic energy (Amari et al. 2003).

tions of prominences and CMEs demonstrated that the magnetic buoyancy force drives the outward motion (Yeh & Wu 1991; Wu & Guo 1997a). Another driver mechanism that can lead to a CME eruption is emerging flux (Chen & Shibata 2000). A number of studies used the shearing of magnetic footpoints to increase the energy of a helmet

streamer, which forces a partial opening-up of the coronal magnetic field to launch a CME (Linker & Mikić 1995; Mikić & Linker 1994; Mikić et al. 1988). However, a fundamental problem of these second-generation MHD models is that the helmet streamer model does not include a magnetic fluxrope.

A third generation of numerical MHD models of CMEs implements the feature of magnetic helical fluxropes (Chen 1997b; Chen et al. 2000; Low & Smith 1993; Low 1994; Guo & Wu 1998; Wu & Guo 1997b; Wu et al. 1995, 1997b,c, 1999; Krall et al. 2000; see example in Fig. 17.3). One model assumes a magnetic fluxrope with footpoints anchored below the photosphere, where an eruption is driven by increasing the poloidal flux (i.e., magnetic flux injection or dynamo model), which can reproduce the dynamics of observed morphological features near the Sun and in magnetic cloud data in interplanetary space (Chen 1989, 1996, 2000; Krall et al. 2000). Another model simulates the evolution of the 3D magnetic field in a current sheet that undergoes magnetic reconnection above a sheared arcade, leading to topological changes with intertwined open fluxtubes (Birn et al. 2000, 2003), similar to the helical fluxropes observed in CMEs. The kink instability leads then to the eruption of sigmoidal (twisted) fluxrope (Fan & Gibson 2003, 2004; Török & Kliem 2003; Török et al. 2004; Kliem et al. 2004). In another model, the combination of photospheric shearing and opposite-polarity emergence is used to produce erupting twisted magnetic fluxropes (Amari et al. 2000; 2003a,b; see Fig. 17.3), similar to the S-shaped (sigmoid) structures observed in soft X-rays. Some MHD simulations focus on the acceleration mechanism of erupting fluxropes, which can be controlled by enhanced magnetic reconnection rates (Cheng et al. 2003).

17.3 Pre-CME Conditions

The cause of a CME is the key for their physical understanding and should be detectable in pre-CME conditions. Once we have a deeper understanding which pre-CME conditions lead to the magnetic instability that drives a CME eruption, we obtain not only a diagnostic but also a predictive tool for the occurrence and evolution of CMEs. Furthermore we can then justify the assumed drivers that have been used in the numerical MHD simulations described in § 17.2. Thus we concentrate in this section on observational signatures of possible CME drivers during pre-CME conditions.

17.3.1 Photospheric Shear Motion

CMEs originate in active regions, which generally exhibit a roughly bipolar field. In order to provide conditions for eruptive phenomena such as flares and CMEs, free magnetic energy needs to be stored in the form of a stressed and sheared field, which is a prerequisite for several CME models (e.g., the dynamo model § 17.1.2 or the tether-straining model § 17.1.5). The stress of the magnetic field can be observationally determined, after removing the 180° ambiguity, by calculating the shear angle between potential field and transverse field vectors from a vector magnetogram (Fig. 17.4), which contains the information of the full 3D magnetic field vectors at the photospheric boundary. This method has been applied to flaring and flare-quiet regions but no dis-

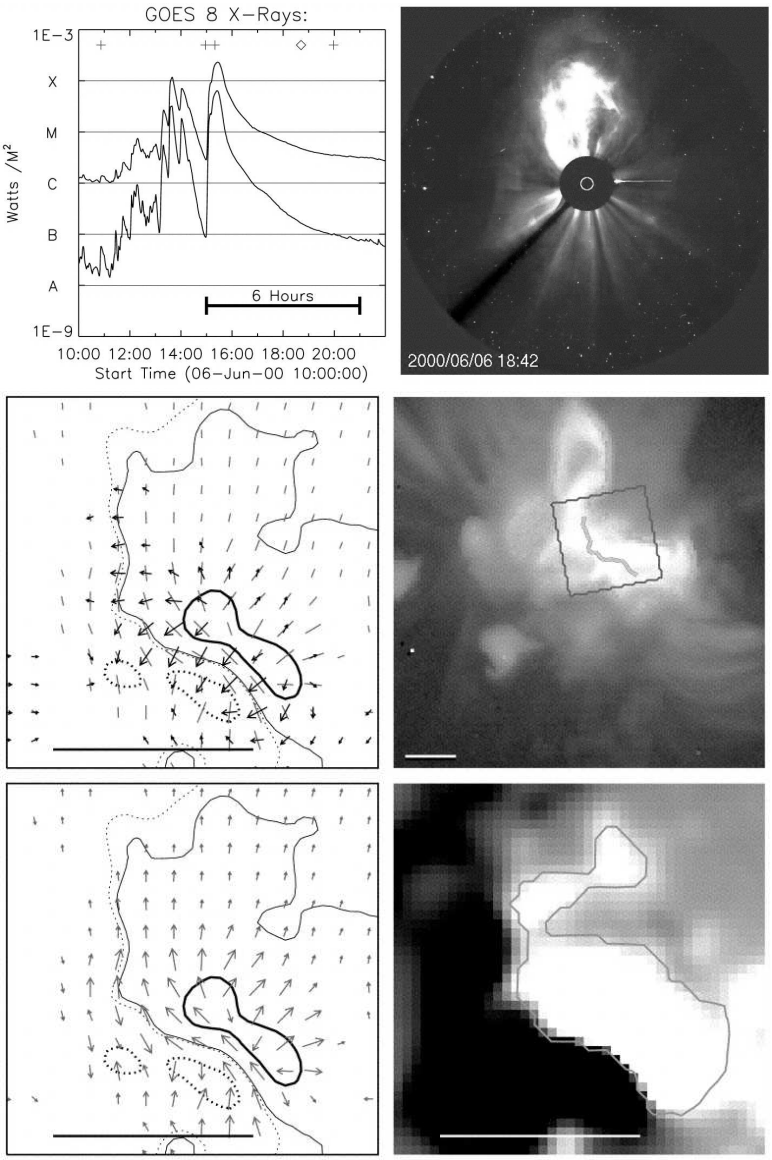

Figure 17.4: GOES soft X-ray light curves (top left) and SoHO/LASCO image (top right) of a halo CME on 2000-Jun-6, 18:42 UT, originating in AR 9026, at heliographic position 21N/14E. Vector magnetograms of AR 9026 are shown in the left panels and soft X-ray *Yohkoh/SXT* images in the right panels in the middle and bottom rows. The contours of the magnetogram are at field strengths of 25 G and 500 G and the magnetic field directions are marked by arrows, with a length proportional to the magnetic field strength of the line-of-sight component (middle left) and the transverse component (bottom left). Note that the magnetic field is highly sheared near the neutral line, with the transverse field almost parallel to the neutral line. The highly sheared segment of the neutral line is overlaid on the *Yohkoh/SXT* image middle right. The spatial scale is indicated with a bar with 50 Mm length (Falconer et al. 2002).

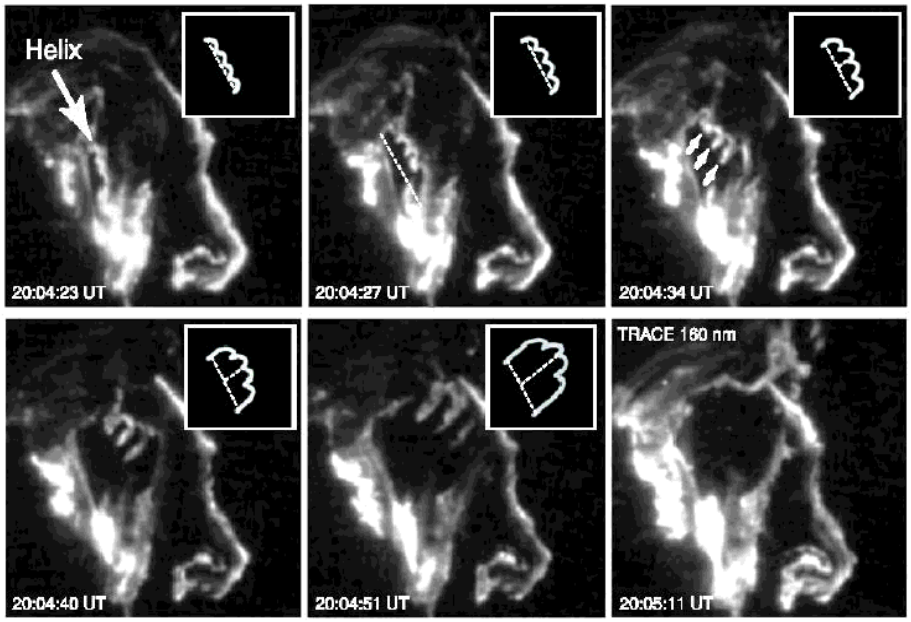

Figure 17.5: TRACE 1600 Åimages in C IV of the GOES-class X3 flare on 2002-Jul-15, 20:04 UT. The inserts illustrate the geometry of the helical structure, exhibiting $3-4$ turns. Note that the helical structure expands, rises, and unwinds during the eruption (Gary & Moore 2004).

criminating differences were found (Leka & Barnes 2003a,b). In a slight variation of this method, the length l_{SS} of the highly sheared segment of the neutral line was evaluated and a correlation was found with the electric current I_N flowing from one polarity to the other, which is a measure of the nonpotentiality of the active region (i.e., $l_{SS} \propto I_N$; Fig. 17.4; Falconer et al. 2001). In a sample of 17 vector magnetograms it was found that this criterion, applied to segments of the neutral line with strong transverse field (> 150 G), yields a viable proxy for the prediction of the CME productivity of an active region (Falconer et al. 2002).

Evidence for a highly sheared magnetic configuration was found to lead to a filament eruption and flare without the presence of a helmet streamer configuration (Cheng & Pallavicini 1984). Theoretical models explain the eruption of a prominence from a sheared magnetic arcade configuration by the formation of helical field lines with subsequent flux cancellation above the neutral line (§ 6.4.1, Fig. 6.15; Van Ballegooijen & Martens 1989; Roumeliotis et al. 1994). The difference of electric conductivities outside and inside the filaments constitutes a magnetic expulsion force (Litvinenko & Somov 2001). Also a change in field-aligned currents can destabilize a filament (Nenovski et al. 2001).

17.3.2 Kink Instability of Twisted Structures

Shearing and stressing of magnetic field lines above the neutral line leads to helical (S-shaped in projection), so-called *sigmoid* structures. Once the helical twist exceeds some critical angle, the structure becomes susceptible to the kink instability, which produces a disruption of the magnetic field leading to the expulsion of a filament or CME. The sigmoidal shape is regarded as an observational signature of azimuthal currents in twisted coronal structures (i.e., loops, arcades, or filaments). The helicity of twisted loops has been found to have a hemispheric preference: forward (reverse) S shapes dominate in the southern (northern) hemisphere (Rust & Kumar 1996). The sense of the sigmoidal shape (forward-S or backward-S) and the handedness of the magnetic twist (left-handed or right-handed; i.e., positive or negative α in force-free fields, see Eq. 5.3.6) have been found to be correlated (Pevtsov et al. 1997). We discussed the magnetic helicity in the context of sigmoidal loops in § 5.5. Recent numerical MHD simulations of the kink instability applied to twisted loops have been performed (e.g., by Fan & Gibson 2003, 2004; Kliem et al. 2004; Török & Kliem 2003, 2004; Török et al. 2004), finding a critical twist number of $1.25\pi \lesssim \Phi_{twist} \lesssim 2.75\pi$ above which no equilibrium exists, consistent with the analytical (force-free) solution $\Phi_{twist} \lesssim 2.49\pi$ of Gold & Hoyle (1960). They investigated also which loop parameters (e.g., twist angle, resistivity, magnetic field gradient with height) lead to quasi-static (stable) non-eruptive expansion, rather than to an eruption. Some twisted filaments have been observed to expand, but failed to erupt (e.g., observed with TRACE on 2002-May-27, 18 UT; Rust 2003; Török & Kliem 2003).

There is now mounting observational evidence that the kink instability indeed plays a prime role for many eruptive filaments, flares, and CMEs (e.g., Canfield et al. 1999; Rust 2001b; Yurchyshyn 2002). Canfield et al. (1999) established statistically that active regions are significantly more likely to be eruptive if they are either sigmoidal or large. A most conspicuous case of a helical fluxtube with multiple turns associated with the double (X3-class) flare event and double CME on 2002-Jul-15 in AR 10030 (Fig. 17.5) has been described by Gary & Moore (2004) and Lui et al. (2003). The erupting helical structure exhibited up to $3-4$ turns (Fig. 17.5; Gary & Moore 2004), and thus is clearly far in the unstable regime of the kink instability. The eruption of the multi-turn helix, however, occurred after the peak of the gyrosynchrotron emission, which is interpreted to be a postreconnection erupting feature below the reconnection region, as one would expect in the *magnetic breakout model.*

17.4 Geometry of CMEs

The geometry of a CME and its dynamic change as a function of time provide the primary input for parameterizing a physical 3D-model. Geometric concepts of CMEs range from semi-spherical shells to helical fluxropes and the observations are often sufficiently ambiguous so that these two opposite concepts cannot easily be discriminated in the data. While CMEs propagating close to the plane of the sky have a relatively simple projected shape, other CMEs propagating in a direction towards the observer have much more complex shapes, the so-called *halo CMEs.* The true 3D configuration is still

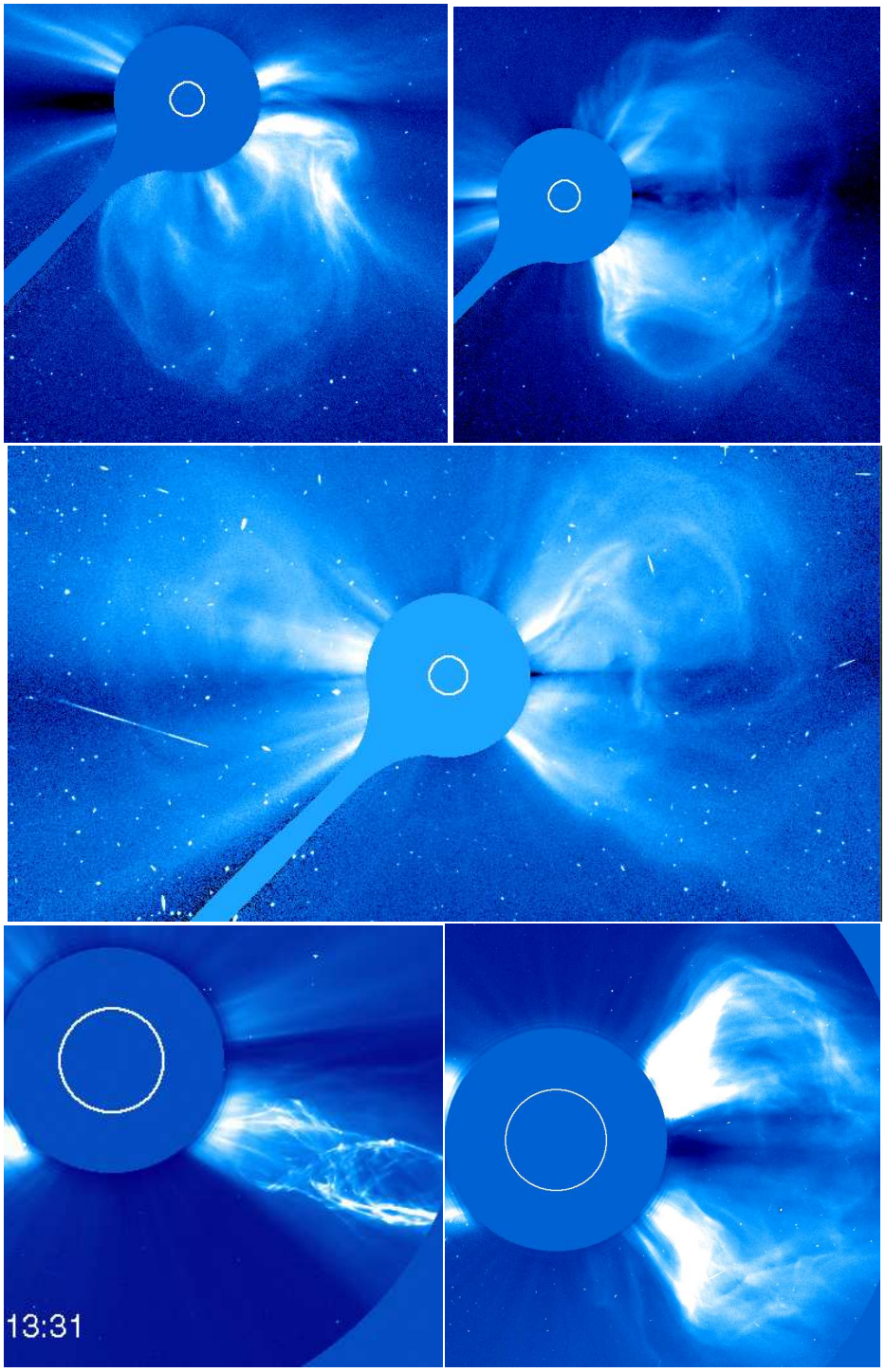

Figure 17.6: LASCO C3 image of a CME on 1998-Mar-29 (top left), a CME of 1998-Apr-20 (top right), a halo CME of 1998-May-6 (middle), an erupting prominence of 1998-Jun-02, 13:31 UT (bottom left), and a large CME of 1997-Nov-06, 12:36 UT (bottom right).

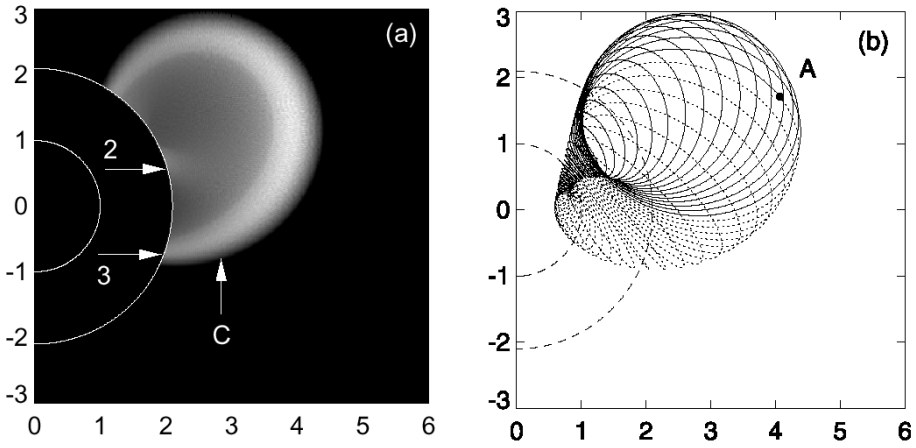

Figure 17.7: Synthetic coronagrph image (a) based on the 3D geometry of a helical fluxrope model (b). Note that the bright leading edge is produced by projection effects (Chen et al. 2000).

unclear due to the difficulties of the optically thin coronal plasma and the highly dynamic nature of CMEs. Coronagraphs measure mainly photospheric photons scattered by free electrons in the coronal plasma (*Thomson scattering*), yielding the integrated density along the line-of-sight, providing us only with a white-light image against the plane of the sky which is not trivial to deconvolve. Geometric inversions are only possible by using strong a priori constraints (e.g., spherical symmetry), while forward-modeling requires very flexible dynamic geometric models. A promising new method to derive the 3D geometry of CMEs has just been developed (at the time when this book went to print) by inversion of the polarization from white-ligth images (Moran & Davila 2004).

First geometric characterizations of CMEs with large statistics have been obtained from *SMM Coronagraph/Polarimeter (C/P)* observations, which includes some 1300 CME events in 1980 and during 1984−1989. There is a large range of angular widths, with an average of $47°$, launched at an average latitude of $35°$ (Hundhausen 1993). A typical characteristic of most CMEs is the three-part structure, consisting of (1) a bright leading edge, (2) a dark void, and (3) a bright core (Illing & Hundhausen 1985). It was suggested that CMEs have a loop-like geometry in a 2D plane, based on close associations of CMEs with eruptive prominences and disappearing filaments (Trottet & MacQueen 1980). Alternatively, 3D geometries were suggested, such as lightbulb bubbles, arcades of loops, or curved and twisted fluxtubes, particularly from *SoHO/LASCO* observations (Fig. 17.6) that became available after 1995 (e.g., Crifo et al. 1983; Schwenn 1986; Webb 1988; MacQueen 1993; Howard et al. 1997; St.Cyr et al. 2000; Vourlidas et al. 2000; Plunkett et al. 2000; Zhao et al. 2002; Gopalswamy et al. 2003; Cremades & Bothmer 2004).

Geometric modeling of CMEs is still in its infancy. Based on the concept of magnetic fluxropes, which consist of helical field lines wound around a curved cylinder (or a segment of a torus), the evolution of a CME is conceived as a steady expansion of

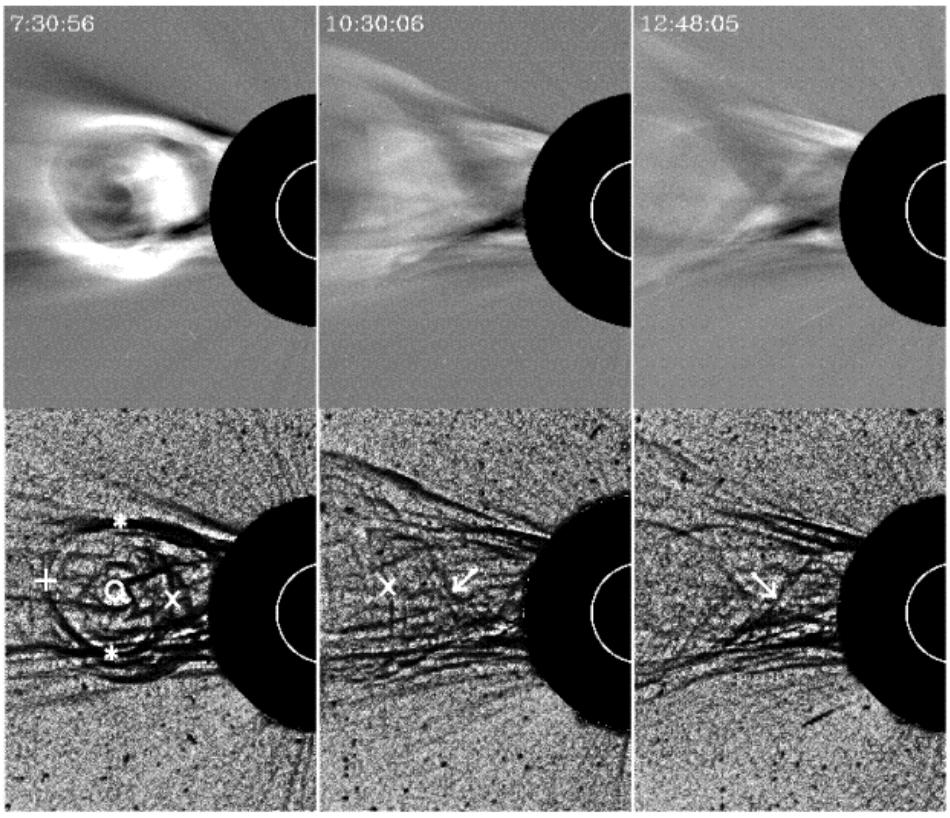

Figure 17.8: LASCO C2 images of the CME of 1997-Apr-30, processed by average-differencing (top row) and edge-enhancing (bottom row). The leading edge is marked +, the trailing edge X, the sides *, and the centroid O. Helical lines (marked with arrows) are seen below the rim that possibly trace the magnetic field (Wood et al. 1999).

this fluxrope into interplanetary space, with the legs connected to the footpoints on the Sun (Chen 1997a). Simulating the Thomson scattering on such a fluxrope structure, a synthetic coronagraph image was then produced (Fig. 17.7) which approximately reproduces the expanding bright leading edge feature of an observed CME (Chen et al. 2000). Edge-enhancing techniques, however, reveal the detailed fine structure of CMEs, which appear to be composed of numerous helical strands (Fig. 17.8, Wood et al. 1999; Fig. 17.9, Dere et al. 1999). Thus, realistic 3D models of CMEs need to disentangle these multiple helical strands, which can be aided by correlation-tracking of time sequences of edge-enhanced images. The kinematic and morphological properties of the CME observed on 1997-Apr-30 and 1997-Feb-23 seem to confirm the concept of erupting fluxrope models (Wood et al. 1999). Comparisons of MHD modeling and observed CME geometries can be found in, for example, Gibson & Low (1998), Andrews et al. (1999), Wu et al. (2000, 2001), and Tokman & Bellam (2002).

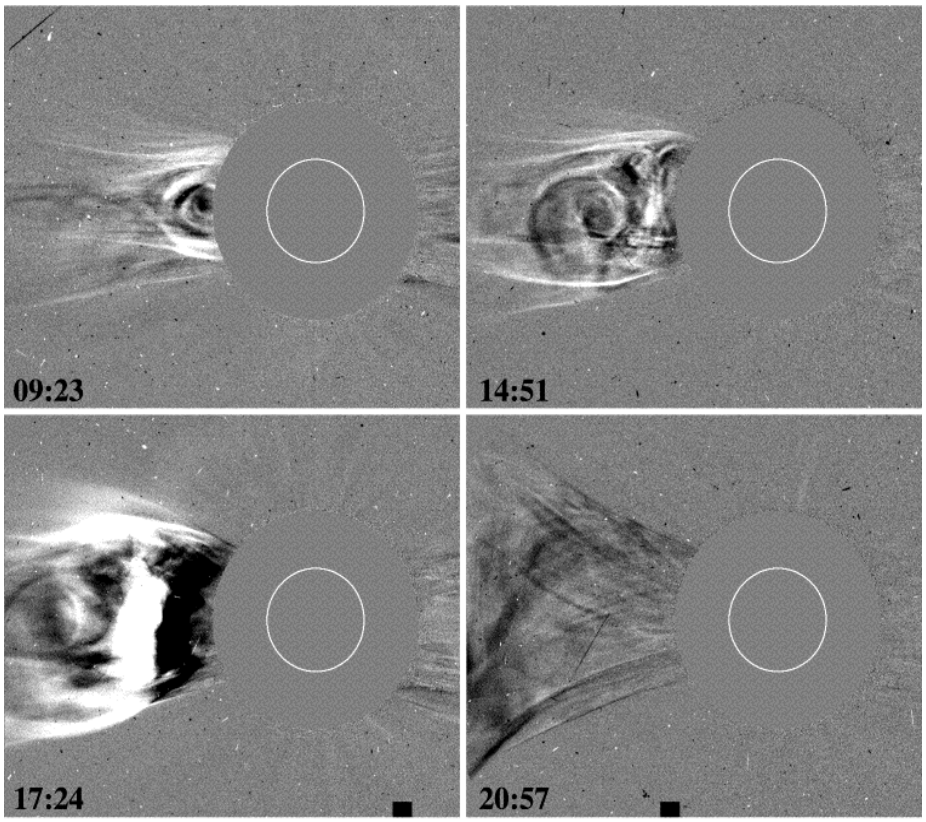

Figure 17.9: LASCO C2 running-difference images of the CME of 1997-Oct-19. The inner circle indicates the solar disk. Note the helical structures in the expanding CME (Dere et al. 1999).

17.5 Density and Temperature of CMEs

17.5.1 Density Measurements of CMEs

The density of CMEs of course is very inhomogeneous and varies by orders of magnitude as a function of the distance from the Sun, or as a function of time. Radial expansion is associated with $n(r) \propto r^{-2}$ for a steady constant expansion speed, or, $n(t) \propto (\mathrm{v}t)^{-2}$ for a time-dependent homologous expansion. Masses of CMEs lay in the range of $m_{CME} \approx 10^{14} - 10^{16}$ g. The density is very inhomogeneously distributed, with the highest density in the compressed plasma at the leading edge, and a comparable mass in the bright core structure inside the cavity (Low 1996). Knowledge of the density and temperature allows estimation of the thermal pressure p_{th} in CME structures, and together with estimates of the magnetic field, one obtains the plasma-β parameter $\beta = p_m/p_{th}$, which provides an important diagnostic of whether the morphology of a CME structure is controlled by the magnetic field or by free radial expansion. Since the radiative loss rate is proportional to the squared density, the

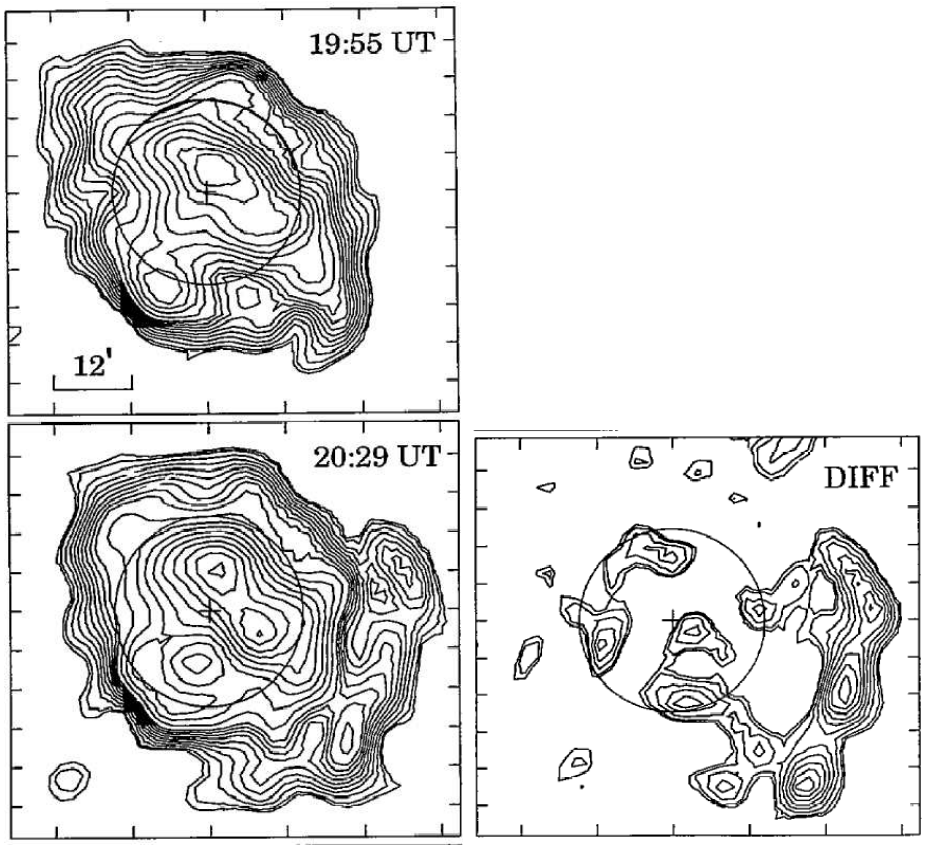

Figure 17.10: Two subsequent radio brightness images and a difference image recorded with the *Clark Lake Radioheliograph* at 73.8 MHz on 1986-Feb-16, before a CME at 19:55 UT, and during the CME at 20:29 UT. The contours range from 15,000 to 300,000 K. The spatial resolution is 4.7 and 5.5 arcmin in E−W and N−S direction, respectively. The radio emission is interpreted as thermal free-free emission from both the quiet Sun corona and from the CME. Note that the difference image subtracts out the quiet Sun component and exhibits the CME leading edge (Gopalswamy & Kundu 1992).

knowledge of the density yields also crucial information on the existence of energy dissipation and heating mechanisms in CMEs. CME masses were mostly estimated from white-light coronagraphs (e.g., Hildner 1977; Poland et al. 1981; Howard et al. 1984). In the following we report on mass estimates of CMEs from two other wavelengths, one in radio (Gopalswamy & Kundu 1992) and one in UV (Ciaravella et al. 2001).

While coronagraphs detect photospheric light that is Thomson-scattered by the CME electrons, radio telescopes can detect thermal bremsstrahlung from CMEs directly. If the brightness temperature of the quiet Sun background (before the CME) is much lower than the brightness temperature of the CME, the background density n_e

can be neglected and the CME density n_{CME} is obtained straightforwardly from the observed brightness temperature T_B

$$T_B = 0.2 T_e^{-1/2} f^{-2} \int_0^\infty (n_e + n_{CME})^2 ds \approx 0.2 T_e^{-1/2} f^{-2} n_{CME}^2 L \qquad (17.5.1)$$

with L the linear dimension of the CME along the line-of-sight. A radio brightness image before and during a CME is shown in Fig. 17.10 (left panels), and the difference image is shown in Fig. 17.10 (right panel). Depending on the line-of-sight depth L, Gopalswamy & Kundu (1992) estimated a CME mass of $m_{CME} = 2.7 - 4.2 \times 10^{15}$ g. With a temperature of $T = 1.0 \times 10^6$ K and an observed brightness temperature of $T_B = 9,7 \times 10^4$ K at $f = 73.8$ MHz, they estimated a mean electron density of $n_{CME} = 0.5 \times 10^6$ cm^{-3} in the frontal leading edge.

There are three common methods to estimate the density of CMEs from UV spectra: (1) Density-sensitive (and temperature-sensitive) line ratios, (2) emission measure method of optically thin plasma, and (3) ratio of collisional excitation rate coefficient ($C_{ex}(T) n_e n_i$) to the radiative scattering rate ($< I_\lambda \sigma_\lambda > n_i$),

$$q = \frac{C_{ex}(T) n_e}{< I_\lambda \sigma_\lambda >} \qquad (17.5.2)$$

where C_{ex} is the excitation rate coefficient, n_e the electron density, n_i the ion density which cancels out in the ratio, I_λ the illuminating flux, and σ_λ the scattering cross section. Using these methods with *SoHO/UVCS* data, a temperature in the range of $T_{CME} \approx 10^{4.5} - 10^{5.5}$ (Ciaravella et al. 2000) and densities in the range of $n_{CME} \approx (1-3) \times 10^7$ cm^{-3} were determined from C III/O VI and N V/O VI ratios at a distance of $R = 1.7 R_\odot$ (Ciaravella et al. 2001).

17.5.2 Temperature Range of CMEs

Most of the CME observations have been made in white light (e.g., with *SMM/C/P* or *SoHO/LASCO*), which provides no temperature information. Many CMEs are also seen in *EUV*, so they must have substantial mass within the temperature range of $T_{CME} \approx 0.5 - 2.0$ MK. Recent observations with *SoHO/UVCS* allow us to narrow down temperature range (e.g., $T_{CME} \approx 10^{4.5} - 10^{5.5}$ from C III, Si III, N V, O VI, and S V line ratios). Coronal mass loss, however, has also been observed at higher temperatures in soft X-ray wavelengths with *Yohkoh/SXT*, which indicates temperatures of $T_{CME} \gtrsim 2$ MK (Hudson & Webb 1997; Hudson 1999). Ciaravella et al. (2000) observe CME plasma at the same time in the intermediate temperature range of $T_{CME} \approx 30,000 - 300,000$ K with *SoHO/UVCS* and with *SoHO/EIT* 195 Å , which has a peak response around $T \approx 1.5$ MK, but argue that the emission seen by EIT 195 Å must result from the sensitivity to cooler temperatures at $T < 0.3$ MK, because cooling plasma would not recombine sufficiently fast to form C III or Si III. On the other hand, prominence material was found to be hot ($T \gtrsim 1.5$ MK) based on similar UVCS diagnostic in Ciaravella et al. (2003) contrary to the assumptions in most CME models, where the core is taken as cold plasma. Thus, more refined work on the temperature diagnostic of CMEs is needed.

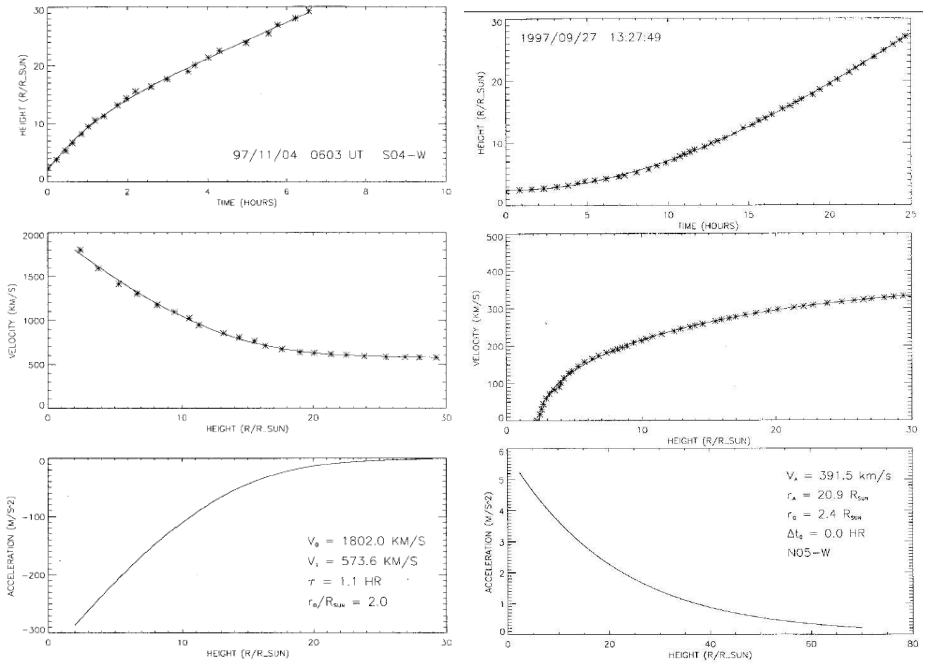

Figure 17.11: Height-time $h(t)$ plot (top), velocity $\mathrm{v}(r)$ (middle), and acceleration profiles $a(r)$ (bottom), as a function of distance $r/R_\odot$, are shown for representants of two different CME classes: a gradual CME with initially negative acceleration (left), and an impulsive CME with initially positive acceleration (right) (Sheeley et al. 1999).

17.6 Velocities and Acceleration of CMEs

The height, velocity, and acceleration of a well-defined CME feature, such as the bright leading edge, are observables that can be measured as a function of time relatively easy, in particular for limb events. The time phases of acceleration reveal the height range where accelerating forces operate, and thus might provide crucial insights into the drivers of CMEs.

Based on the observed characteristics of CME velocity $\mathrm{v}(t)$ and acceleration profiles $a(t)$ observed with *SoHO/LASCO* over the distance range of $r = 2 - 30\ R_\odot$ it was proposed that there exist two distinct classes of CMEs (Sheeley et al. 1999): (1) *gradual CMEs*, apparently formed when prominences and their cavities rise up from below coronal streamers, typically attaining slow speeds ($\mathrm{v} \approx 400 - 600$ km s^{-1}) with clear signs of gradual acceleration ($a = 3 - 40$ m s^{-2}) at distances $R < 30 R_\odot$; and (2) *impulsive CMEs*, often associated with flares and Moreton waves on the visible disk, with speeds in excess of $\mathrm{v} \gtrsim 750 - 1000$ km s^{-1}, observed to have a constant velocity or decelerating at distances $R \gtrsim 2 R_\odot$ when first seen in coronagraphs (Sheeley et al. 1999). An example of each class is given in Fig. 17.11: a gradual CME shows initially positive acceleration (Fig. 17.11, left), while an impulsive CME shows ini-

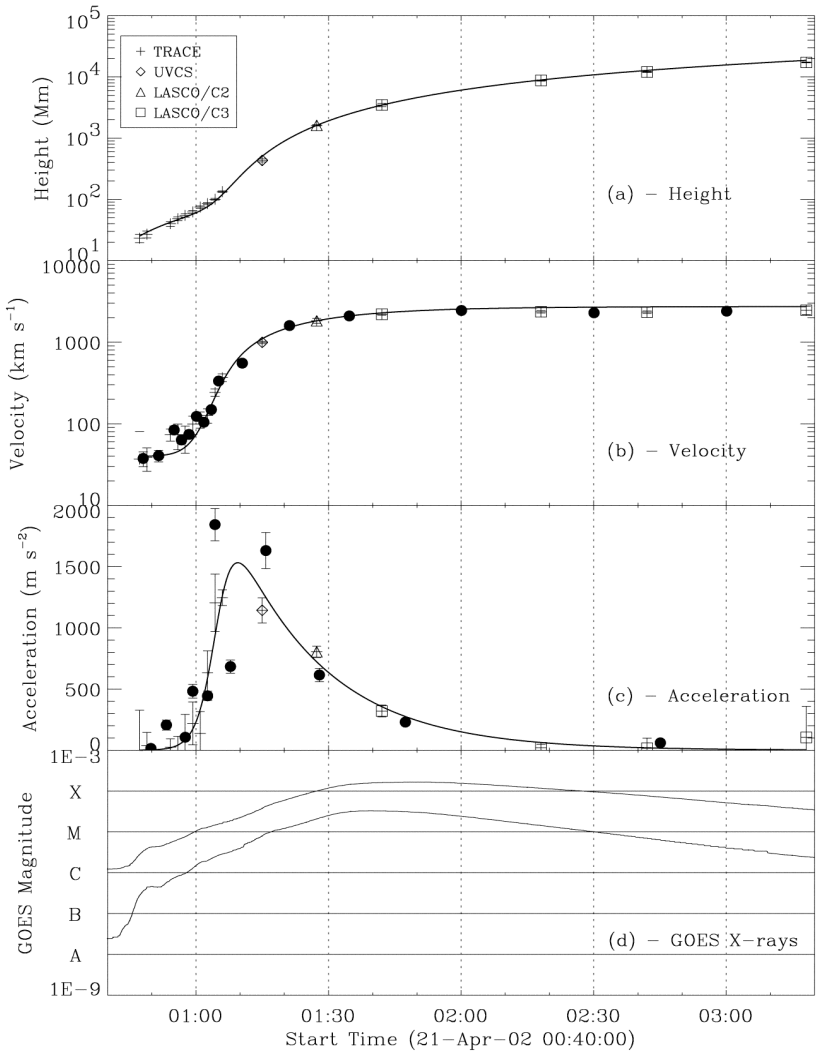

Figure 17.12: Height-time $h(t)$, velocity $v(t)$, and acceleration $a(t)$ profiles as well as GOES-10 soft X-ray flux profiles for a CME observed with TRACE, UVCS, and LASCO during the 2002-Apr-21, X1.5 GOES-class flare, shown during the interval of 00:47–03:20 UT. The solid lines are the best fits using Eqs. 17.6.2–4 (Gallagher et al. 2003).

tial negative acceleration (Fig. 17.11, right). Sheeley et al. (1999) found also that the (Earth-directed) halo versions of the two classes appear as smooth halos (for gradual CMEs) or more ragged structures (for impulsive CMEs).

The observations in Fig. 17.11 suggest that the acceleration profile $a(t)$ can be approximated by either an exponentially increasing or decreasing function, (e.g., Sheeley

et al. 1999),

$$a(t) = a_0 \exp\left[-(t - t_0)/t_a\right] . \tag{17.6.1}$$

The velocity profile $\mathrm{v}(t)$ follows then from integrating the acceleration profile $a(t)$,

$$\mathrm{v}(t) = \mathrm{v}_0 + \int_{t_0}^{t} a(t)\, dt\, , \tag{17.6.2}$$

and the height-time profile $h(t)$ from double integration of the acceleration profile $a(t)$,

$$h(t) = h_0 + \mathrm{v}_0 (t - t_0) + \int_{t_0}^{t} \int_{t_0}^{t} a(t)\, dt\, dt\, . \tag{17.6.3}$$

The acceleration profile of CMEs cannot be observed at low heights ($R \lesssim 2R_\odot$) with coronagraphs. However, coordinated measurements in EUV can fill in this gap. A coordinated observation of a CME with TRACE, UVCS, and LASCO revealed both the initial acceleration as well as the later deceleration phase (Fig. 17.12). So the acceleration profile shown in Fig. 17.12 could be fitted with a combined function of exponentially increasing and decreasing acceleration (Gallagher et al. 2003),

$$a(t) = \left[\frac{1}{a_r \exp\left(t/\tau_r\right)} + \frac{1}{a_d \exp\left(t/\tau_d\right)}\right]^{-1} . \tag{17.6.4}$$

The CME event shown in Fig. 17.12 reaches a final speed of $\mathrm{v} \approx 2500$ km s^{-1}, which is among the fastest 1% CME speeds observed with LASCO. The start of the acceleration at 00:47 UT coincides with the start of hard X-ray emission at energies ≥ 25 keV, while the maximum of acceleration at 01:09 UT coincides with the peak of the ≥ 25 keV hard X-ray emission, which suggests a close causal connection between the energy release and CME driving force.

A remarkable observation of a CME event of 1998-Apr-23 05:29 UT has been reported in soft X-rays (Alexander et al. 2002). A variable acceleration model fitted to the data yields a peak acceleration of $a \approx 4865$ m s^{-2} within the first $0.4R_\odot$, which is comparable with the largest reported CME accelerations. Also unusual is the detection in soft X-ray wavelengths, and it is not clear whether the accelerated soft X-ray plasma represents a fluxrope, shock front, or corresponds to other identifiable parts of a CME seen in white light.

A quantitative model for the acceleration of CMEs was developed by Chen & Krall (2003), based on a 3D magnetic fluxrope model (Fig. 17.13, left). The accelerating force $\mathbf{F}$ can be integrated over a toroidal section of the fluxrope from the MHD momentum equation (Eq. 6.1.17),

$$\mathbf{F} = -\nabla p - \rho \mathbf{g} + \mathbf{j} \times \mathbf{B}\, . \tag{17.6.5}$$

This model predicts a universal scaling law where maximum acceleration is attained shortly after the expanding loop passes the height

$$Z_* = \frac{S_f}{2}\, , \tag{17.6.5}$$

where S_f is the footpoint separation distance of the magnetic fluxrope. An example of the application of this model to an observed CME (1997-Feb-23) is shown in Fig. 17.13 (right).

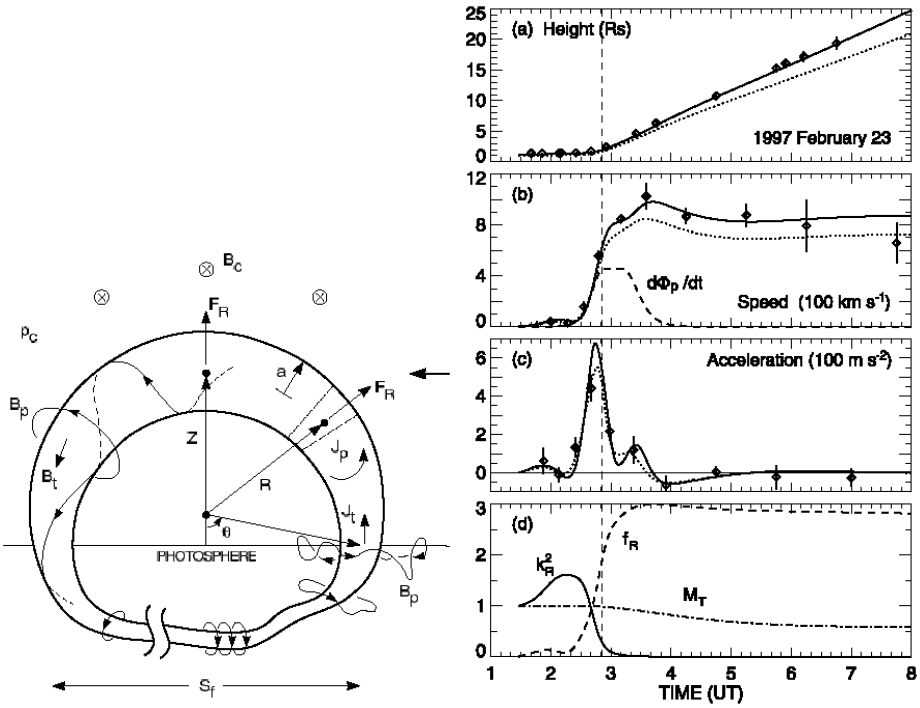

Figure 17.13: Height-time $h(t)$, velocity $\mathrm{v}(t)$, and acceleration $a(t)$ profiles fitted from a magnetic fluxrope model to LASCO observations of the 1997-Feb-23 CME event. The solid curve corresponds to the leading edge and the dotted curve to the centroid of the expanding fluxrope. The vertical line indicates the time when the CME reached $2R_\odot$ from the Sun center. The leading edge attains a maximum speed of $\mathrm{v} = 1000$ km s^{-1}. A schematic of the magnetic fluxrope model is shown on the left-hand side, indicating the footpoint separation distance S_f and the height Z of the fluxrope centroid (Chen & Krall 2003).

17.7 Energetics of CMEs

A key question is how the required (magnetic) energy storage is achieved and how it is released to produce a CME. The energetic problem has been pointed out by the Aly–Sturrock conjecture (Aly 1984; Sturrock 1991), which implies that a closed force-free magnetic field has less energy than the equivalent fully open field (with an identical photospheric boundary condition). This conjecture severely constrains the occurrence of a CME in a force-free corona if the magnetic field is the primary driver of the eruption. There are three groups of CME models that satisfy this constraint: (1) the pre-CME magneto-static corona is not force-free and cross-field currents are present (Wolfson & Dlamini 1997); (2) the CME involves magnetic flux from several flux systems so that most of the involved field is not opened, such as in the *magnetic breakout model* (Antiochos 1998, Antiochos et al. 1999b); or (3) the CME includes a detached fluxrope (Low 1996). The magnetic energy of a CME can be estimated to some ex-

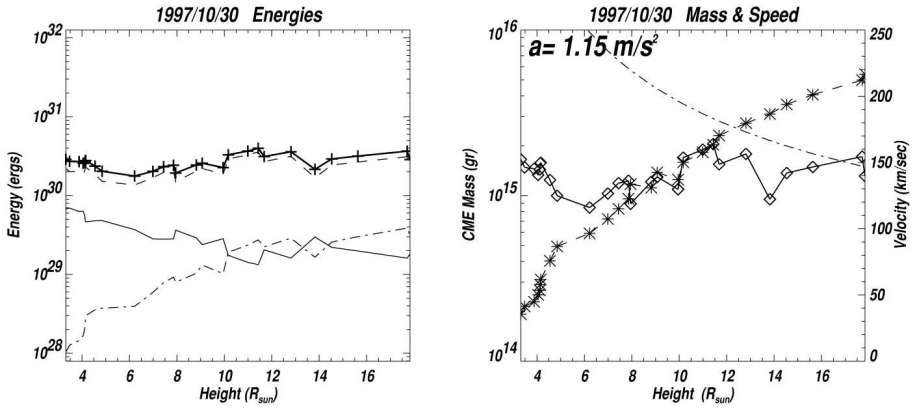

Figure 17.14: LASCO measurements of the evolution of the potential energy (dashed line), kinetic energy (dash-dotted line), magnetic energy (solid lines), and total energy (solid line with crosses) of the CME of 1997-Apr-30 (left frame). The evolution of the CME mass (solid line with diamonds), center-of-mass speed (dashed line with asterisks), and the derived acceleration (dash-dotted line) are shown in the right frame (Vourlidas et al. 2000).

tent from integrating the extrapolated 3D magnetic field over the volume of the CME, but these extrapolations are problematic since the force-free extrapolations are given inputs of the observed photospheric field unlikely to be potential or force-free (Metcalf et al. 1995).

One approach to obtain a better understanding of the dynamical evolution of physical parameters in an erupting CME is the study of the energy budget. A recent study (Vourlidas et al. 2000) indicates that some of the accelerating fluxrope CMEs have conservation of their total energy (i.e., the sum of magnetic, kinetic, and gravitational potential energy is constant; see example in Fig. 17.14, left). In this study, white-light intensities I_{obs}, velocities v_{CME}, and angular widths of CMEs were measured from LASCO observations at distances of $R = 2.5 - 30\ R_\odot$. The mass of a CME is estimated from the ratio of the excess observed brightness I_{obs} (from difference images) to the brightness $I_e(\vartheta)$ of a single electron at angle ϑ from the plane of the sky, which is computed from the Thomson scattering function (Billings 1966). Assuming a standard abundance of fully-ionized hydrogen with 10% helium, the CME mass is

$$m_{CME} = \frac{I_{obs}}{I_e(\vartheta)}\ \mu\ m_p \approx \frac{I_{obs}}{I_e(\vartheta)}\ 2 \times 10^{-24}\ (\mathrm{g})\ . \qquad (17.7.1)$$

The potential energy ε_{grav} of the fluxrope is defined by the amount of energy required to lift its mass from the solar surface, that is,

$$\varepsilon_{grav}(R) = \sum_{fluxrope} \int_{R_\odot}^{R} \frac{GM_\odot m_i}{r_i^2}\ dr_i\ , \qquad (17.7.2)$$

where m_i and r_i are the mass and distance from the Sun center, respectively, for each pixel in the observed difference image. The kinetic energy ε_{kin} is integrated over the

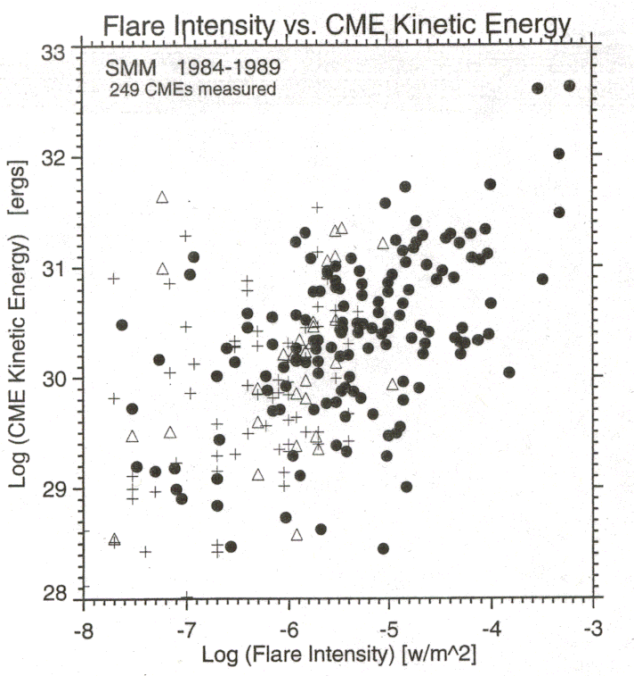

Figure 17.15: A logarithmic scatterplot of kinetic energies of CMEs and the peak intensities of associated X-ray flares seen in the GOES integrated soft X-ray flux. The sample includes 249 CME events observed with *SMM C/P* (Hundhausen 1997).

CME area,

$$\varepsilon_{kin}(R) = \frac{1}{2} \sum_{fluxrope} m_i \mathrm{v}_{CME}^2 \,. \tag{17.7.3}$$

The magnetic energy is assumed to vary during propagation according to the conservation of the magnetic flux, $B(R) \times A(R) = const$, where A is the area of the fluxrope. Expressing the volume with $V = Al$, where l is the length of the fluxrope, the magnetic energy ε_{mag} can be estimated as,

$$\varepsilon_{mag}(R) = \frac{1}{8\pi} \int_{fluxrope} B^2(R) dV \approx \frac{1}{8\pi} \frac{l}{A} (B \times A)^2 \,, \tag{17.7.4}$$

where an average value of the magnetic flux is $< B \times A >= 1.3 \pm 1.1 \times 10^{21}$ G cm^2, obtained from several magnetic clouds observed with the *Wind* spacecraft during 1995−1998 at Earth distance (Lepping et al. 1990). With this method Vourlidas et al. (2000) analyzed the energy budget of 11 CMEs and found that the kinetic energy is smaller than the potential energy for relatively small CMEs, but larger for relatively fast CMEs ($\mathrm{v}_{CME} \geq 600$ km s^{-1}). The magnetic energy advected by the fluxrope is converted into kinetic and potential energy for relatively slow CMEs, so that the total

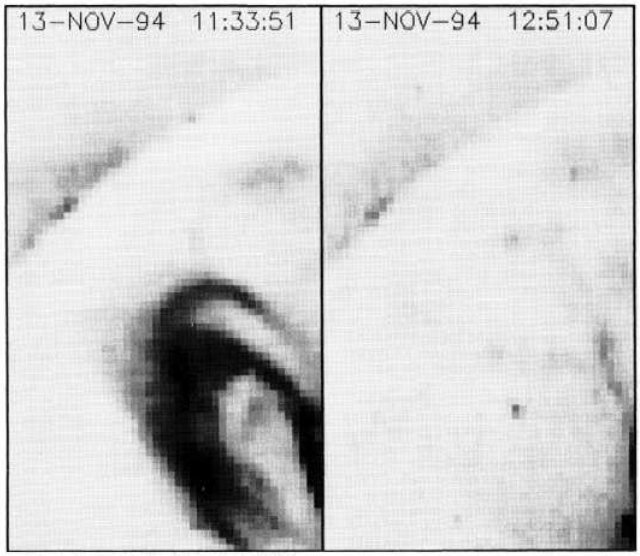

Figure 17.16: Yohkoh/SXT images of a long-duration flare at beginning (left) and after (right) the impulsive flare phase, located in the northeast of the solar disk. Note that most of the flare loops disappear almost completely from the field-of-view as a result of their outward motion (Hudson et al. 1996).

energy is constant, $\varepsilon_{tot} \approx \varepsilon_{grav} + \varepsilon_{kin} + \varepsilon_{mag}$. Thus, the slow CMEs are magnetically driven. For relatively fast CMEs ($v_{CME} \geq 600$ km s^{-1}) the magnetic energy is significantly below the potential and kinetic energy. Typical total energies of CMEs are $\varepsilon_{tot} \approx 10^{29} - 10^{32}$ erg, which is comparable with the range of flare energies estimated from nonthermal electrons (Fig. 9.27). The kinetic energies of CMEs from a larger sample of 294 events is shown in Fig. 17.15, demonstrating an approximate correlation with the total soft X-ray flux and a similar energy range as nonthermal flare energies (Hundhausen 1997). Moore (1988) estimated the energy of CMEs from the nonpotential magnetic energy stored in twisted fluxropes and found similar values (i.e., $\Delta\varepsilon_{twist} \approx 10^{30} - 10^{32}$ erg).

17.8 Coronal Dimming

A powerful diagnostic of the early phase of CMEs is the so-called *coronal dimming*, which is often detectable as a relative deficit of coronal mass or emission measure compared with pre-CME conditions, interpreted as a vacuum-like rarefaction after the launch or "evacuation" of a CME. The effect of coronal dimming is most dramatically seen on the solar disk, but is also detectable above the solar limb in some cases. We discussed the effect of CME dimming previously in the context of global waves (§ 8.3), which originate at CME launch sites and propagate more or less spherically over the solar surface, displaying a density compression at the wavefront and a rar-

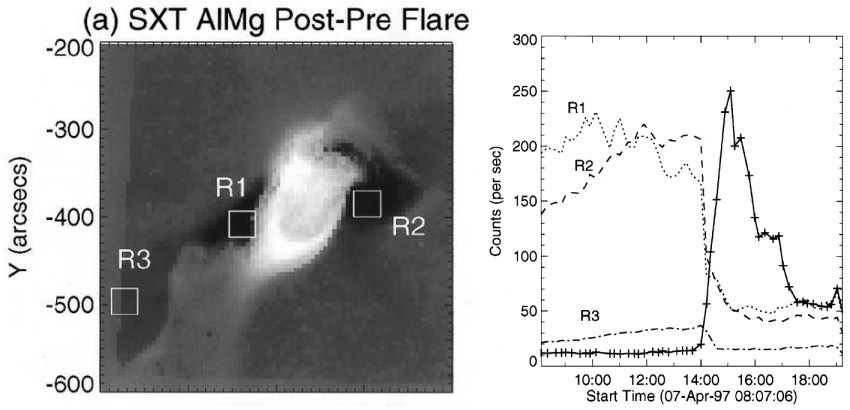

Figure 17.17: *Yohkoh/SXT* Al/Mg difference image of the 1997-Apr-07, 13:50 UT, flare, with the difference taken before (13:28:42 UT) and after (17:40:40 UT). Three spatial locations with notable dimming in soft X-rays are marked with R1, R2, and R2 (left), and the corresponding light curves are shown from *SoHO/EIT* 195 Å (right panel) and compared with the (anti-correlated) flare light curve (thick solid line in right panel) (Zarro et al. 1999).

efaction behind the wavefront. Such waves have been called *Moreton waves* and *EIT waves* (§ 8.3.1) and have been simulated based on theoretical models (§ 8.3.2). Here we concentrate on observations that relate the effect of coronal dimming more specifically to the occurrence of CMEs.

Coronal dimming occurs after a CME launch and were first described as *abrupt depletions of the inner corona* using the HAO K-coronameter data (Hansen et al. 1974), or as a *transient coronal hole* (Rust 1983), using *Skylab* data (Rust & Hildner 1978).

Let us review coronal dimming observed in soft X-ray wavelengths. The disappearance of soft X-ray-bright loops in the long-duration flare of 1994-Nov-13, 11:30 UT, has been witnessed (Fig. 17.16) by Hudson et al. (1996). The disappearance and associated dimming was interpreted as a consequence of outward motion rather than as a cooling process, based on the fact that the radiative cooling time was estimated to be much longer than the disappearance (dimming) time. This event is considered as an example for the counterpart of a CME seen in soft X-rays, with an estimated mass loss of $> 4 \times 10^{14}$ g and a temperature of $T \gtrsim 2.8$ MK (Hudson et al. 1996). A dimming was also observed just prior to a "halo" CME on 1997-Apr-07, using *Yohkoh/SXT* (Fig. 17.17; Sterling & Hudson 1997; Zarro et al. 1999). Here the strongest dimming occurred symmetrically at both sides of the flare volume, close to the ends of a pre-flare S-shaped sigmoid (Sterling & Hudson 1997). The resulting dimmings in these regions persisted for more than 3 days following the flare. At the same time, a dramatic dimming was also noticed in EUV, using the *SoHO/EIT* 195 Å Fe XII images (Zarro et al. 1999). The locations of reduced EUV intensity are co-spatial and simultaneous with those of soft X-ray dimming features. The EIT light curves show a drop down to ≈25% of the preflare flux, and are clearly anti-correlated with the flare flux (Fig. 17.17, right). The cause of EUV and SXR coronal dimmings were interpreted

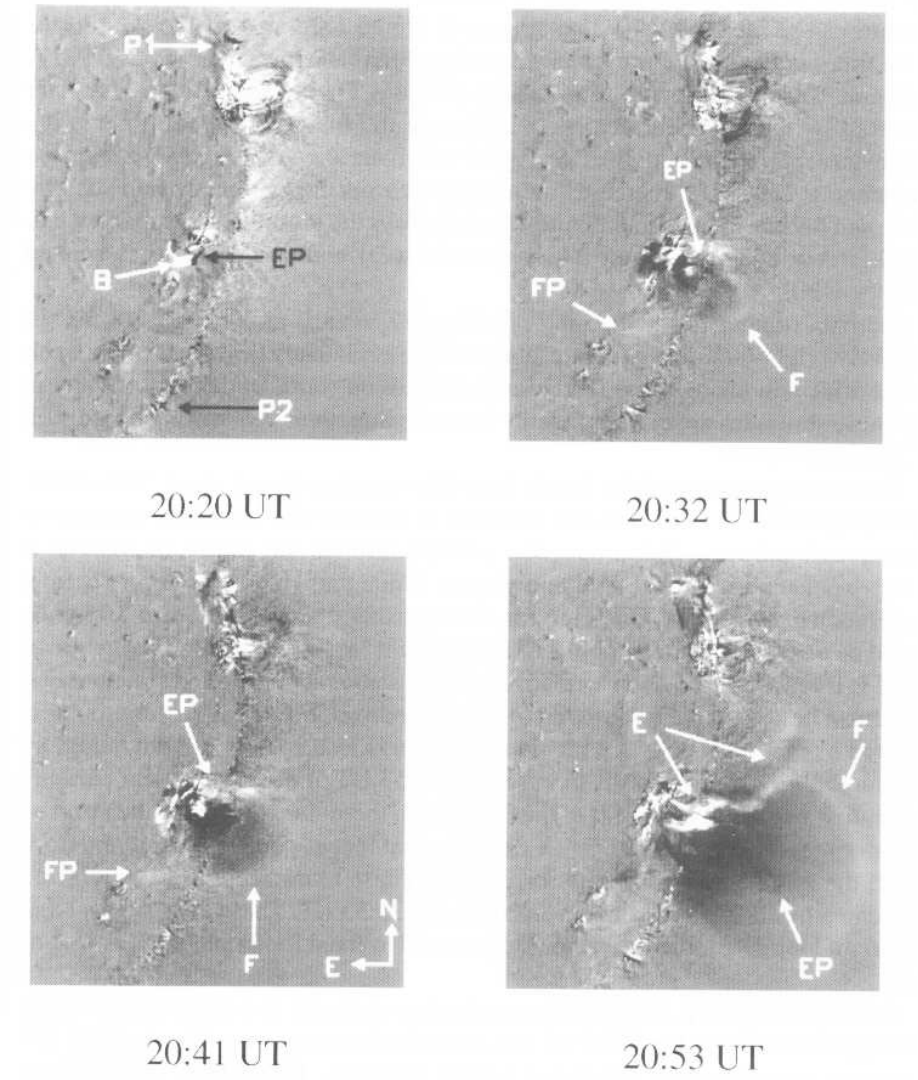

Figure 17.18: EIT running difference images of the initiation of a CME. EP=eruptive prominence, B=flare-like brightening, F=outer front of CME, FP=footpoint of one side of CME, and E=secondary set of ejecta. Note the location of strongest dimming at the center of the expanding CME bubble (Dere et al. 1997b).

within the framework of a fluxrope eruption, partially controlled by the CME.

The dimming at the launch time of a CME is most conspicuously observed in EUV, generally associated with a spherically expanding wave over the global solar surface (§ 8.3; e.g., Thompson et al. 1999). Probably the clearest record of the vertical structure of coronal dimming regions during the launch of a CME can be seen in the EIT 195 Å observations of 4 time frames during the CME of 1996-Dec-23, 20:20 UT (Fig. 17.18; Dere et al. 1997b). The onset of the dimming appears to be coincident with the ini-

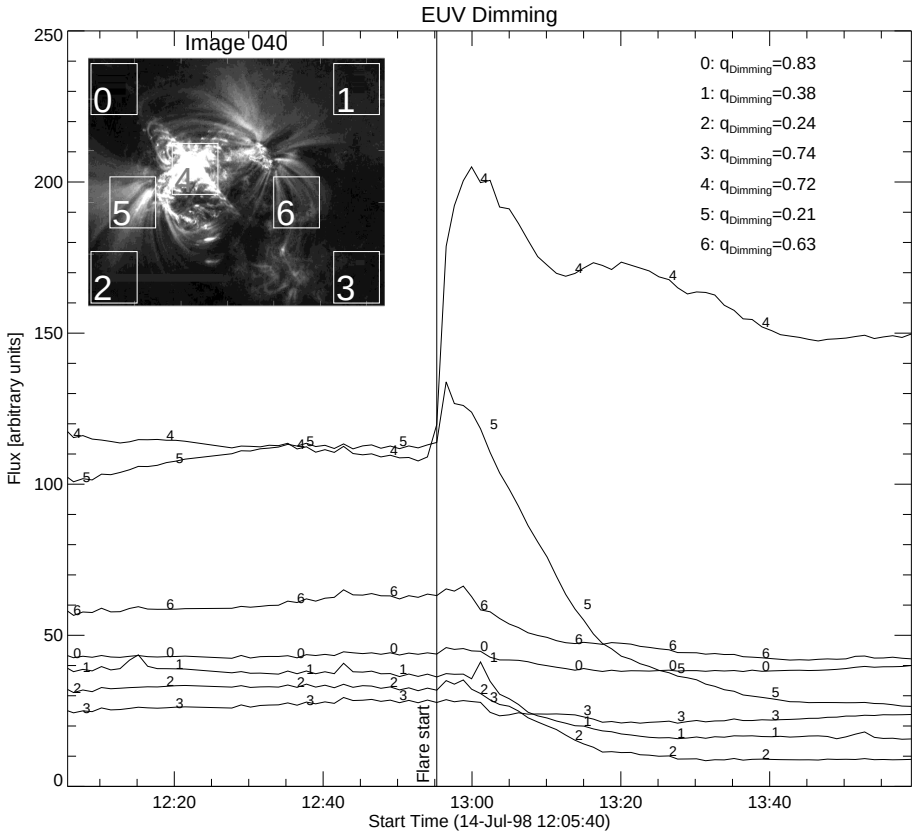

Figure 17.19: EUV dimming measured during the 1998-Jul-14, 12:55 UT, Bastille-Day flare with TRACE 171 Å. Note that the strongest dimming is aligned with the dipole axis of the active region (positions 1, 2, and 5). The numbered light curves correspond to the EUV fluxes integrated over the numbered boxes in the inserted map. The center location of the flare coincides with the center of the diffraction pattern (Aschwanden et al. 1999b).

tiation of global EIT waves, usually continues for hours thereafter, and can exhibit a quite asymmetric and skewed distribution regarding the center of origin (Thompson et al. 1998a), or even forming channels of irregular shapes (Chertok & Grechnev 2003). An analysis of 7 fast (> 600 km s^{-1}) CMEs corroborated that the coronal dimmings generally map out the apparent footprints of the CMEs observed in white light (Thompson et al. 2000b). The coronal dimming after a CME launch was found to coincide in EUV and Hα (Thompson et al. 2000a; Jiang et al. 2003). The Hα dimming is thought to be associated with the material evacuated near the feet of the erupted fluxrope (Jiang et al. 2003). This dipolar symmetry of EUV dimming has also been observed during the 1998-Jul-14, 12:55 UT, Bastille-Day flare, where the strongest dimming (down to a level of 21%$-$38% of the preflare flux) occurred near the leading and following polar-

ity of the dipolar active region, while the dimming was much less pronounced (at a level of 63%−83% of the preflare flux) in orthogonal directions (Fig. 17.19; Aschwanden et al. 1999b; Chertok & Grechnev 2004).

A multi-wavelength study with a broad temperature coverage between 20,000 K and 2 MK using CDS data showed that the dimming after a CME is strongest for plasma with a temperature of ≈ 1.0 MK, and thus the evacuated material comes from coronal heights rather than from transition region heights (Harrison & Lyons 2000). Spectroscopic evidence that coronal dimming at CME onsets represent indeed material outflows (rather than temperature changes) has been proven by measurements of Doppler shifts (e.g., with a velocity of $\mathrm{v} \approx 30$ km s^{-1} in coronal Fe XVI and Mg IX lines co-spatial with dimming regions; Harra & Sterling 2001). Another line of evidence that dimming corresponds to mass loss (rather than temperature changes) comes from mass loss estimates, which have been found to agree between white-light emission (observed with LASCO) and EUV dimming (observed with CDS), in the range of $m_{CME} \approx 5 \times 10^{13} - 4 \times 10^{15}$ g (Harrison et al. 2003). Also the comparison of the ejected material ($\approx 6 \times 10^{15}$ g) of an eruptive prominence observed in microwaves was found to be comparable with the coronal dimming ($\approx 1.7 \times 10^{15}$ g) estimated from soft X-ray data (Gopalswamy & Hanaoka 1998).

17.9 Interplanetary CME Propagation

Most of the coronal phenomena described in this book occur at a distance of $1R_\odot < r \lesssim 2R_\odot$ from the Sun center. The propagation of CMEs has been observed in white light by using coronagraphs (e.g., with *SoHO/LASCO*, in the range of $2R_\odot \lesssim r \lesssim 30R_\odot$). Many space-based observations of CME-related phenomena are performed from satellites in an Earth orbit, at a distance of 1 AU (i.e., $r \approx 200\ R_\odot$). The physics of interplanetary and heliospheric phenomena (which is beyond the scope of this book) entails a plethora of plasma physics processes equally as rich as coronal phenomena, and are described in a number of textbooks and monographs (Russell et al. 1990; Schwenn & Marsch 1991a,b; Kivelson & Russell 1995; Crooker et al. 1997; Song et al. 2001; Balogh et al. 2001; Carlowicz & Lopez 2002). In the following section we sketch a short overview of physical concepts that connect coronal to interplanetary CME phenomena. A subset of these phenomena that play a role in solar-terrestrial connectivity are also referred to as *space weather phenomena* (Song et al. 2001), of which the geoeffictive ones (e.g., *solar storms*; Carlowicz & Lopez 2002), are of utmost interest for the inhabitants on Earth.

17.9.1 Interplanetary Magnetic Field (IMF)

The *heliospheric 3D magnetic field* is defined by the flow of the solar wind. The field in the regions between the planets near the ecliptic plane is more specifically called the *interplanetary magnetic field*. The basic geometry of the interplanetary magnetic field has the form of an Archimedian spiral, as inferred by Parker (1963b) from the four assumptions: (1) the solar wind moves radially away from the Sun at a constant speed; (2) the Sun rotates with a constant period (i.e., with a synodic period of 27.27

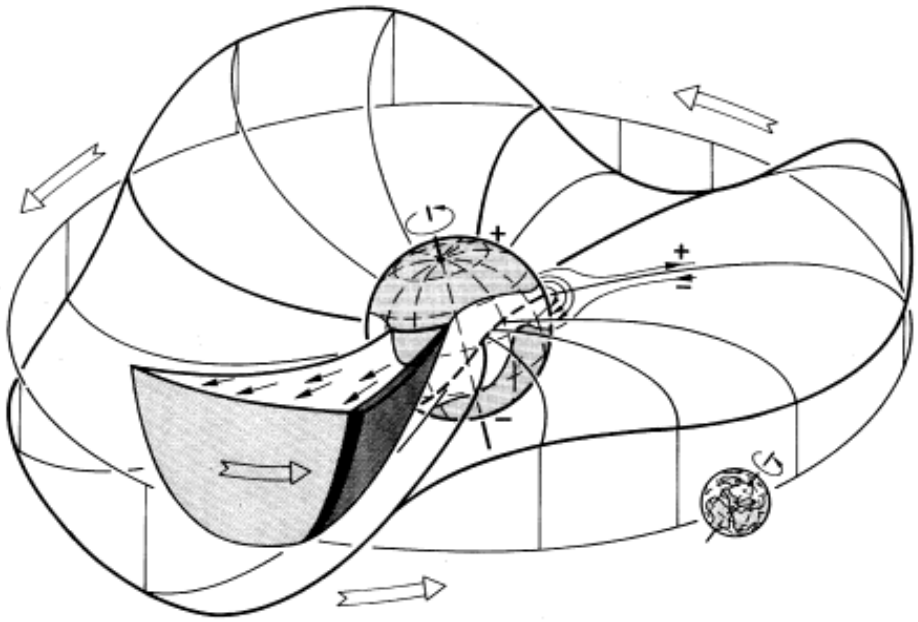

Figure 17.20: The interplanetary magnetic field has a spiral-like radial field and the boundary layer between the two opposite magnetic polarities in the northern and southern hemispheres is warped like a *"ballerina skirt"*. This concept was originally suggested by Hannes Alfvén in 1977.

days at the prime meridian defined by Carrington); (3) the solar wind is azimuthally symmetric with respect to the solar rotation axis; and (4) the interplanetary magnetic field is frozen-in the solar wind and anchored at the Sun. The solar wind stretches the global, otherwise radial field into spiral field lines with an azimuthal field component. The resulting Archimedian spirals leave the Sun near-vertically to the surface and cross the Earth orbit at an angle of $\approx 45°$. Measurements of the magnetic field direction at Earth orbit reveal a *two-sector pattern* during the period of declining solar activity and a *four-sector pattern* during the solar minimum, with oppositely directed magnetic field vectors in each sector. From this ecliptic cut, a warped heliospheric current sheet can be inferred that has the shape of a *"ballerina skirt"* (Fig. 17.20). The solar axis is tilted by $7.5°$ to the ecliptic plane, and the principal dipole magnetic moment of the global field can be tilted by as much as $\approx 20° - 25°$ at activity minimum, and thus the warped sector zone extends by at least the same angle in northerly and southerly direction of the ecliptic plane. A longitudinal cut of the solar magnetic field near the Sun is shown in Fig. 1.14, based on a model by Banaszkiewicz et al. (1998).

The strength of the interplanetary magnetic field, of course, depends on the solar cycle (§ 1.3), varying between $B \approx 6$ nT and 9 nT (10^{-5} G) at a distance of 1 AU. The interplanetary magnetic field can be heavily disturbed by flare-related shocks and

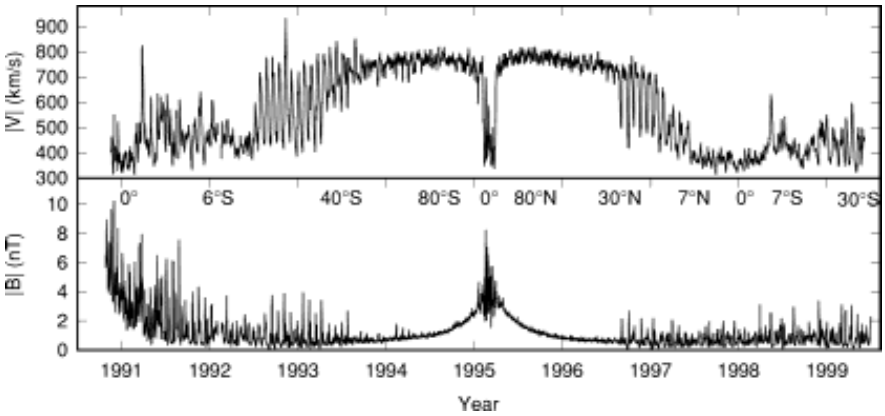

Figure 17.21: The solar wind speed as a function of heliographic latitude (upper panel) and the magnitude of the magnetic field as a function of time (lower panel) measured by *Ulysses* from launch through its first solar orbit. Note the detection of the slow solar wind ($v \approx 400$ km s^{-1}) in low latitudes ($\lesssim 20°$) and of the fast solar wind ($v \approx 800$ km s^{-1}) in high latitudes ($\gtrsim 20°$) (Balogh 2001).

propagating CMEs. The magnetic field is near-radial near the Sun and falls of with $B(R) \approx R^{-2}$ there, while it becomes more azimuthal at a few AU and falls of with $B(R) \propto R^{-1}$ at larger heliocentric distances according to the model of Parker. Reviews on the interplanetary magnetic field can be found in, for example, Kivelson & Russell (1995; § 4), Burlaga (2001), Ness (2001), Russell (2001), and Schwenn & Marsch (1991a).

17.9.2 Solar Wind

Parker's (1958) theoretical model of the solar wind (§ 4.10; Fig. 4.33) predicts that the coronal plasma outflow expands into a supersonic solar wind, which was confirmed by measurements of *in situ* spacecraft, such as with *Mariner II* in 1962, or with *Ulysses* more recently (Fig. 17.21). The transition into a supersonic wind occurs at $r \approx 5\ R_\odot$. However, the model of Parker (1958) does not address the energy equation and cannot explain the slow and fast solar wind components. The energy balance equation yields a different solution for open field regions, where the fast solar wind originates, and for the corona over closed field regions, where the slow solar wind originates (see shaded area in Fig. 1.14). In magnetically closed regions, downward heat conduction is the dominant energy loss mechanism. In open field regions, energy is taken out with the solar wind in the forms of work done against gravity and kinetic energy of the flow (Table 9.1). Of course, the exact solution of the energy balance equation depends also on the coronal heating function, which is not known. However, to obtain a fast solar wind of $v \approx 800$ km s^{-1}, energy needs to be deposited far out in the corona (e.g., by dissipation of Alfvén waves; see § 9.4). Furthermore, the energy deposition is also different for electrons and ions, as measured by the higher ion temperature in the solar wind, compared with the electron temperature (Fig. 9.13). The solar wind flow speed

is usually much larger than the local sound speed or Alfvén speed, typically having a Mach number of ≈ 10, which implies that the dynamic pressure is much higher than both the magnetic pressure and the thermal pressure. The magnetic field is frozen-in in the solar wind flow due to the high conductivity.

CMEs represent transient activities that disturb the solar wind. The average CME speed is slightly below the solar wind speed in the corona. The CME plasma is entrained in the interplanetary magnetic field lines and is transported into the solar wind. Various signatures of CMEs in the solar wind include: (1) transient interplanetary shock waves, (2) He abundance enhancements, (3) unusual ionization states (e.g., He^{+}), (4) brief density enhancements and long-duration density decreases, (5) proton and electron temperature depressions, (6) bi-directional field-aligned flows of halo electrons and low-energy protons, and (7) magnetic field variations associated with *magnetic clouds* or *fluxropes*. The chemical abundance and charge state compositions have been found to be systematically different in CMEs and in the background solar wind.

Reviews on the solar wind and CME disturbances of the solar wind can be found in, for example, Holzer (1989), Schwenn & Marsch (1991a,b), Gosling (1994, 1996), Goldstein et al. (1995), Hundhausen (1995), Winterhalter et al. (1996), Schwadron et al. (1997), Burgess (1997), Neugebauer et al. (2001), Leer (2001), Schwenn (2001), Marsch (2001), Webb (2001), Habbal & Woo (2001), Balogh (2001), Russell (2001), Balogh et al. (2001), Bochsler (2001), Matthaeus (2001b), Esser (2001), Kunow (2001), Cranmer (2002a,b), Ofman (2003), Erdoes (2003).

17.9.3 Interplanetary Shocks

CMEs have typical propagation speeds of $\mathrm{v} \approx 300 - 400$ km s^{-1}, but fast CMEs have been measured up to speeds of $\mathrm{v} = 2000$ km s^{-1}. Since the fast solar wind has a typical speed of $\mathrm{v} \approx 800$ km s^{-1}, fast CMEs are supersonic. Thus, such fast CMEs can drive transient interplanetary shocks. Numerical simulations with HD or MHD codes (for instance see Fig. 17.22), have been able to reproduce the observed speeds and pressure profiles of shocks and CME events out to large distances from the Sun. In such simulations, a pressure pulse is initiated in the lower corona. As the front of a fast CME overtakes the slower solar wind, a strong gradient develops and pressure waves steepen into a forward shock propagating into the ambient wind ahead, and occasionally a reverse shock propagates back through the CME towards the Sun. Numerical simulations of CMEs propagating from the corona through the heliosphere can be found in, for example, Mikić & Linker (1994); Linker & Mikić (1995); Linker et al. (2001); Odstrčil et al. (1996, 2002), Toth & Odstrčil (1996), and Odstrčil & Pizzo (1999a,b).

There are a number of complications that can occur, such as the fact that a faster CME can catch up with a slower CME and interact. Such interactions form compound streams in the inner heliosphere. These systems continually evolve further and merge with other CMEs and shocks as they move outward. In the outer heliosphere, beyond 5 AU, such structures form *merged interaction regions*, which become so extensive that they encircle the Sun like a distant belt. Such regions block and modulate galactic cosmic rays (i.e., the flux of high-energy particles that continuously streams into the

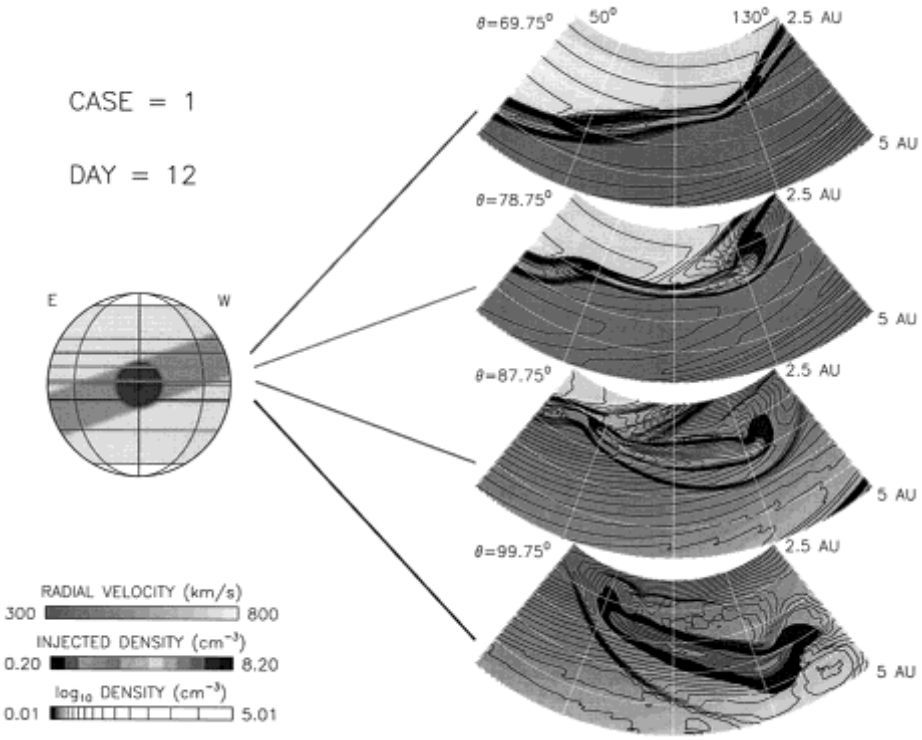

Figure 17.22: Numerical MHD simulations of a CME moving through the ambient solar wind. The CME is injected in the center of the heliospheric current sheet streamer belt (left), which is tilted to the solar axis. The propagating CME is shown at slices in heliolongitude and at a distance of 2.5-5 AU from the Sun 12 days after launch. The slices are 4 different heliolatitudes and show how the CME's shape, pressure and speed vary depending on the ambient solar wind conditions (Courtesy Victor Pizzo, NOAA/SEC).

heliosphere). Finally, a forward interplanetary shock wave that passes the Earth's magnetosphere may cause a sudden commencement of a *magnetic storm* or *substorm* at the Earth and change the electrical and magnetic connection of the interplanetary magnetic field with the Earth's magnetic field. Reviews on interplanetary shocks, CMEs, and related phenomena can be found in, for example, Schwenn & Marsch (1991a,b), Kivelson & Russell (1995), Burlaga (1995), Colburn & Sonett (1996), Crooker et al. (1997), Balogh & Riley (1997), Whang et al. (1998), Balogh et al. (2001), Song et al. (2001), Lepping (2001), and literature referenced therein.

17.9.4 Solar Energetic Particles (SEP)

Solar energetic particle (SEP) events refer to accelerated particles detected in the heliosphere. Some originate in solar flares, while others are accelerated in transient interplanetary shocks, as they are produced by fast CMEs. The acceleration mechanisms

are basically the same types we discussed in § 11.5 on shock acceleration. Solar energetic particle events are classified into two types, *gradual* and *impulsive* SEP events, depending on their energy versus time profile. *Gradual SEP events* occur with a rate of ≈ 10/year during the maximum of the solar cycle, each one can last several days, and they are likely to be accelerated directly in interplanetary shocks rather than by flares in the corona. *Impulsive SEP events* occur more frequently, with a rate of ≈ 100/year during the maximum of the solar cycle, they last only a few hours, and they are much weaker than gradual SEP events. Since they originate along magnetic field lines connected to coronal flare sites, their acceleration could be governed by the same magnetic reconnection process that governs the associated flare. Because their ^{3}He/^{4}He ratio is much higher than in the normal solar wind, they are also called ^{3}He-rich events. Interplanetary particles can also be accelerated in the electric fields that are generated at *co-rotating interaction regions (CIR)* between high-speed and low-speed streams. To some extent, the location where acceleration of interplanetary particles takes place can be determined from the velocity dispersion (i.e., time-of-flight effects), $t_{prop} = L/\mathrm{v}$, of particles arriving at Earth.

Literature on solar energetic particle events can be found in, for example, Kahler et al. (1984), Reames & Stone (1986), Reames et al. (1988, 1991a,b, 1992, 1994; 1996, 1997, 2001a,b), Reames (1990b, 1995a,b, 1999, 2001a,b, 2002), Gosling (1993), Kahler (1992, 1994, 2001), Tylka (2001), Reames & Tylka (2002), and references therein.

17.9.5 Interplanetary Radio Bursts

There are two sources of energetic particles in interplanetary space, either flare-related magnetic reconnection sites in the solar corona that are connected to interplanetary space via open field lines, or shock acceleration sites associated with supersonic CME fronts that propagate through interplanetary space. Since the plasma in interplanetary space is collisionless, superthermal and high-energy particles can propagate unimpeded through interplanetary space and form particle beams (e.g., electron beams or ion beams). The beam free energy is converted into Langmuir waves, and some Langmuir wave energy is converted to radio waves at the fundamental or harmonic local plasma frequency (§ 15.1, 15.4). Thus, beam-driven type III-like radio bursts are common in interplanetary space (Fig. 15.13), and occasionally there occur also type IV-like radio bursts (i.e., synchrotron emission caused by energetic electrons confined in a magnetic trap created behind an interplanetary shock wave). The spatial size of interplanetary radio bursts can be very large, since the extent of the radio source grows with distance from the Sun. However, interplanetary type III emission is not produced continuously along the propagation path of electron beams, but rather seem to occur in localized, unresolved regions of the interplanetary medium. There occur also interplanetary type II-like bursts, also called *shock-associated (SA)* events, believed to be produced by collisionless shock waves associated with passing CMEs. Thus, interplanetary radio bursts provide a rich diagnostic on the acceleration and propagation of energetic particles and shock waves. However, only radio bursts with plasma frequencies $\gtrsim 20$ MHz (above the Earth's ionospheric cutoff frequency) can be observed with ground-based radio telescopes, which extends only out to about $1 - 2$ solar radii, while all interplan-

etary radio bursts further out have lower plasma frequencies and require space-based radio detectors.

Reviews on interplanetary radio bursts can be found in, for example, Lin (1974), Simnett (1986b), Dulk (1990), Schwenn & Marsch (1991), Robinson (1997), Aschwanden & Treumann (1997), Cairns et al. (2000), Reiner (2001), and Bougeret (2001).

17.10 Summary

Coronal Mass Ejections (CMEs) are a new eruptive phenomenon distinct from flares although they are related by the common solar magnetic fields that produce them. Both eruptions involve releases of magnetic energy in comparable magnitudes. CMEs and flares represent complementary phenomena, both being produced as by-products of a common magnetic instability that is controlled on a larger scale in the solar corona. Theoretical models include five categories: (1) thermal blast models, (2) dynamo models, (3) mass loading models, (4) tether release models, and (5) tether straining models (§ 17.1). Numerical MHD simulations of CMEs are currently produced by combinations of a fine-scale grid that entails the corona and a connected large-scale grid that encompasses propagation into interplanetary space, which can reproduce CME speeds, densities, and the coarse geometry (§ 17.2). The trigger that initiates the origin of a CME seems to be related to previous photospheric shear motion and subsequent kink instability of twisted structures (§ 17.3). The geometry of CMEs is quite complex, exhibiting a variety of topological shapes from spherical semi-shells to helical fluxropes (§ 17.4), and the density and temperature structure of CMEs is currently investigated with multi-wavelength imagers (§ 17.5). The height-time, velocity, and acceleration profiles of CMEs seems to establish two different CME classes: gradual CMEs associated with propagating interplanetary shocks, and impulsive CMEs caused by coronal flares (§ 17.6). The total energy of CMEs (i.e., the sum of magnetic, kinetic, and gravitational energy), seem to be conserved in some events, and the total energy of CMEs is comparable to the energy range estimated from flare signatures (§ 17.7). A closely associated phenomenon to CMEs is coronal dimming, which is interpreted in terms of an evacuation of coronal mass during the launch of a CME (§ 17.8). The propagation of CMEs in interplanetary space (which is beyond the scope of this book), provides diagnostic on the heliospheric magnetic field, the solar wind, interplanetary shocks, solar energetic particle (SEP) events, and interplanetary radio bursts (§ 17.9).